

Learning Regularization Functionals for Inverse Problems: A Comparative Study

Johannes Hertrich^{a,b,*} Hok Shing Wong^{c,*} Alexander Denker^d
 Stanislas Ducotterd^e Zhenghan Fang^f Markus Haltmeier^g
 Željko Kereta^d Erich Kobler^h Oscar Leongⁱ
 Mohammad Sadegh Salehi^j Carola-Bibiane Schönlieb^k
 Johannes Schwab^l Zakhar Shumaylov^k Jeremias Sulam^f
 German Shâma Wache^m Martin Zach^e Yasi Zhangⁱ
 Matthias J. Ehrhardt^{c,†} Sebastian Neumayer^{m,†}

In recent years, a variety of learned regularization frameworks for solving inverse problems in imaging have emerged. These offer flexible modeling together with mathematical insights. The proposed methods differ in their architectural design and training strategies, making direct comparison challenging due to non-modular implementations. We address this gap by collecting and unifying the available code into a common framework. This unified view allows us to systematically compare the approaches and highlight their strengths and limitations, providing valuable insights into their future potential. We also provide concise descriptions of each method, complemented by practical guidelines.

1 Introduction

Inverse problems are ubiquitous in imaging sciences. As an example, [magnetic resonance imaging \(MRI\)](#) and X-ray [computed tomography \(CT\)](#) play a central role in many modern applications. Mathematically, the reconstruction is commonly modeled as a linear inverse problem [125]. More precisely, we want to reconstruct an (unknown) image $\mathbf{x} \in \mathbb{R}^d$ from an observation $\mathbf{y} \in \mathbb{R}^m$ determined by the linear relation

$$\mathbf{y} = \mathbf{H}\mathbf{x} + \mathbf{n}, \quad (1)$$

where $\mathbf{H} \in \mathbb{R}^{m \times d}$ encodes the underlying data acquisition process and the noise $\mathbf{n} \in \mathbb{R}^m$ accounts for imperfections in this description. As \mathbf{H} is often ill-conditioned or non-invertible, the inverse problem (1) is ill-posed in the sense of Hadamard [64] and reconstructing \mathbf{x} from \mathbf{y} is challenging.

^aUniversité Paris Dauphine-PSL, FR ^bInria Paris, FR ^cUniversity of Bath, UK ^dUniversity College London, UK ^eÉcole Polytechnique Fédérale de Lausanne, CH ^fJohns Hopkins University, Baltimore, US ^gUniversity of Innsbruck, AT ^hJohannes Kepler University Linz, AT ⁱUniversity of California, Los Angeles, US ^jIndependent Scholar, UK ^kUniversity of Cambridge, UK ^lUniversity of Applied Sciences Kufstein, AT ^mChemnitz University of Technology, DE
 *joint first author †joint last author

A classical method to address ill-posedness is variational regularization, for which the unknown \mathbf{x} is approximated by

$$\hat{\mathbf{x}}(\mathbf{y}) = \arg \min_{\mathbf{x}} \{D(\mathbf{Hx}, \mathbf{y}) + \alpha R(\mathbf{x})\}. \quad (2)$$

In (2), the data fidelity $D: \mathbb{R}^m \times \mathbb{R}^m \rightarrow \mathbb{R}$ ensures data consistency, the regularizer $R: \mathbb{R}^d \rightarrow \mathbb{R}$ promotes desired properties of \mathbf{x} , and the regularization parameter $\alpha > 0$ balances the two. There is a vast zoo of regularizers R in the literature [135]. A prominent example is the (anisotropic) **total variation (TV)** [131] $R(\mathbf{x}) = \|\nabla \mathbf{x}\|_1$, which measures the ℓ_1 -norm of the discretized gradient. The variational approach (2) leads to several desirable properties, e.g.,

- **universality:** different forward and noise models can be incorporated;
- **data consistency:** the reconstruction $\hat{\mathbf{x}}(\mathbf{y})$ satisfies (1) approximately, with control provided by the regularization parameter α ;
- **stability:** the data-to-reconstruction map $\mathbf{y} \mapsto \hat{\mathbf{x}}(\mathbf{y})$ is often continuous. Namely, the noise \mathbf{n} is not arbitrarily amplified in the reconstruction;
- **interpretability:** the regularization functional R can be analyzed.

The literature on mathematical analysis for variational regularization methods is vast, see [23, 77, 135] and the references therein.

In many situations, the variational approach (2) has a Bayesian interpretation. There, the solution to the inverse problem (1) is formally defined as the posterior distribution of possible reconstructions \mathbf{x} given some measurement \mathbf{y} . To this end, the image $\mathbf{x} \in \mathbb{R}^d$ is modeled as a realization of a random variable $X \sim \mathbb{P}_X$. Reconstruction of \mathbf{x} from \mathbf{y} is then addressed by analyzing the posterior $\mathbb{P}_{X|Y}$, which can be expressed via Bayes' theorem as

$$\mathbb{P}_{X|Y}(\mathbf{x} | \mathbf{y}) \propto \mathbb{P}_{Y|X}(\mathbf{y} | \mathbf{x}) \mathbb{P}_X(\mathbf{x}). \quad (3)$$

The conditional distribution $\mathbb{P}_{Y|X}$ is usually available as it is induced by \mathbf{H} and the noise distribution. Consequently, the challenge lies in finding accurate models of the prior \mathbb{P}_X . In our finite-dimensional setting, it is natural to assume that the distributions $\mathbb{P}_{X|Y}$, $\mathbb{P}_{Y|X}$, and \mathbb{P}_X admit densities with respect to the Lebesgue measure, which we denote by $p_{X|Y}$, $p_{Y|X}$, and p_X . There exist various statistical estimators of the posterior $p_{X|Y}$. Among them, the **maximum a-posteriori (MAP)** estimator of X given $Y = \mathbf{y}$, defined as

$$\arg \max_{\mathbf{x} \in \mathbb{R}^d} p_{X|Y}(\mathbf{x} | \mathbf{y}) = \arg \min_{\mathbf{x} \in \mathbb{R}^d} \{-\log p_{Y|X}(\mathbf{y} | \mathbf{x}) - \log p_X(\mathbf{x})\}, \quad (4)$$

recovers the variational problem (2) with $p_{Y|X}(\mathbf{y} | \mathbf{x}) \propto \exp(-D(\mathbf{Hx}, \mathbf{y}))$ and $p_X(\mathbf{x}) \propto \exp(-\alpha R(\mathbf{x}))$. A second popular choice is the **minimum mean-squared-error (MMSE)** estimator, which can be shown to be the *expectation* of the posterior $p_{X|Y}$ rather than its maximum.

Over the past years, deep-learning-based approaches have become the state-of-the-art for solving inverse problems and there are many excellent reviews [15, 63, 111, 148]. Although they achieve impressive results, several concerns regarding their trustworthiness remain. Recent works reveal troublesome issues that may arise for deep-learning-based approaches if the aforementioned *desirable properties* are not met [9, 54]. In contrast, hand-crafted regularizers R such as **TV** are theoretically founded but cannot achieve the same reconstruction quality as data-driven approaches. We focus on the blend of these approaches, namely the learning of R from data. Occasionally, we write R_θ to emphasize the dependence on the parameters θ . Below, we give a brief overview of the state-of-the-art in the learning of regularizers. In Sections 2 and 3, we go into more detail for the regularizers and training methods contained in this comparison.

A pioneering learnable regularizer R is the **fields of experts (FoE)** [130], which is the sum of 1D potentials composed with convolutional filters. Recently, it was proposed to learn the **FoE** using linear splines, leading to the **convex ridge regularizer (CRR)** [55] and **weakly-convex ridge regularizer**

(WCRR) [56]. Another convex architecture is the **input-convex neural network (ICNN)** [15] and its descendant, the input weakly-convex neural network [138]. Following the idea of structured nonconvexity, these were extended to **input difference-of-convex neural networks (IDCNNs)** [160]. Examples of more complex multi-scale **convolutional neural network (CNN)** regularizers are the **total deep variation (TDV)** [82], the **least-squares residual (LSR)** [163], and energy-based generative priors [155]. An alternative with the emphasis on sparse representations is dictionary learning [29, 94, 143]. Such models are generalized to neural networks using a nonlinear representation via generative models [4, 28, 46, 62].

A parallel development aims to instead learn the proximal operator

$$\text{prox}_R(\mathbf{x}) = \arg \min_{\mathbf{z}} \left\{ \frac{1}{2} \|\mathbf{x} - \mathbf{z}\|_2^2 + R(\mathbf{z}) \right\}, \quad (5)$$

of R , which is central to proximal algorithms for solving (2). The interpretation of prox_R as a variational denoiser has inspired the popular **plug-and-play (PnP)** approaches [51, 70, 87, 115, 124, 145, 157], which replace the prox_R in proximal algorithms with a learned denoiser. Under certain conditions on its architecture, an underlying R exists [50, 75]. Since this R is only given implicitly, we are limited to proximal algorithms for solving (2) and tracking the objective values is difficult. As an example, we discuss **learned proximal networks (LPNs)** in Section 2.8.

Given a parametric regularizer R_θ , we need to learn its parameters θ from data. Towards this goal, many paradigms have been introduced over the past decades. One notable paradigm is bilevel learning, which adapts the θ such that the reconstruction (2) minimizes some loss. This idea started with learning only the regularization parameter α in (2) [31, 39, 40, 60, 85], and has been gradually lifted to learning regularizers. The required gradients of the reconstructions with respect to θ can be computed via implicit differentiation [78, 92, 164], leading to the **bilevel learning with implicit differentiation (BL-IFT)** approach. In practice, the optimization problem in (2) is only solved up to a certain precision. The **method of adaptive inexact descent (MAID)** [132] and related works [114, 133] explicitly capture this inaccuracy. If we instead use backpropagation to compute the gradients, the resulting method is commonly known as unrolling [99]. As the memory requirements grow linearly with the number of iterations of the deployed optimization algorithm, this is impractical in our setting. Instead, we can deploy **bilevel learning with Jacobian free backpropagation (BL-JFB)** [27, 52] as efficient intermediate regime.

A second paradigm is based on distinguishing desirable and undesirable images a priori, without actually solving (2). This is reminiscent of classification with two classes. Prominent examples include contrastive divergence [155], **adversarial regularization (AR)** [93, 101] and **network Tikhonov (NETT)** [91]. During training, these approaches are not linked to the variational problem (2), and require the selection of a suitable regularization parameter α for the inverse problem at hand.

A third paradigm arises from the Bayesian viewpoint (3) and the interpretation of (2) as the **MAP** estimator. Under this framework, learning R amounts to estimating the prior p_X . Several authors construct R by leveraging generative models [68, 151]. To reduce the computational effort and required data, **expected patch log-likelihood (EPLL)** [162], **local adversarial regularization (LAR)** [122] and **patch normalizing flow regularizer (PatchNR)** [5] propose to instead approximate a patch distribution, see [116] for an overview. Alternatively, we can approximate p_X by the density $p_\sigma := p_{X_\sigma}$ of $X_\sigma = X + \sigma\eta$ with $\eta \sim \mathcal{N}(0, I)$. Then, R can be learned with a denoising loss via Tweedie's formula [98, 126], which links p_σ with the **MMSE** estimator of X given X_σ . The resulting training method is called **score matching (SM)** and several variants have been proposed [76, 80, 128, 147, 154]. Tweedie's formula also induces the popular gradient-step denoiser [37, 74, 127].

Outline In Section 2, we review existing regularization architectures. In Section 3, we discuss the training methodologies, ranging from bilevel learning to contrastive learning, and distribution matching approaches. Section 4 describes the setup for our numerical comparison. In particular, this includes the optimization algorithm, forward models, datasets, and evaluation metrics. Section 5

Table 1: Regularizer architectures and their parameter count as implemented for this chapter.

	Convex	Parameters	Backbone	Reference	Description
CRR	✓	≈ 15k	CNN	[55]	Section 2.1
WCRR	✗	≈ 15k	CNN	[56]	Section 2.1
ICNN	✓	≈ 26k	CNN	[101]	Section 2.3
IDCNN	✗	≈ 53k	CNN	[160]	Section 2.4
EPLL	✗	≈ 280k	dictionary learning	[162]	Section 2.5
PatchNR	✗	≈ 3M	normalizing flow	[5]	Section 2.5
CNN	✗	≈ 200k	CNN	[122]	Section 2.5
TDV	✗	≈ 400k	UNet	[82, 83]	Section 2.6
LSR	✗	≈ 4M	DRUNet	[163]	Section 2.7
LPN	✗	≈ 4M	UNet	[50]	Section 2.8

presents the numerical results, which are discussed and interpreted in Section 6. There, we also outline limitations and possible extensions. Finally, conclusion are drawn in Section 7.

2 Overview of Regularizer Architectures

First, we review various regularization architectures, which are summarized in Table 1. These architectures vary in terms of parameter count, complexity, and convexity properties. For algorithmic convenience, we focus on differentiable R , though all architectures can be used with non-smooth activations. Unless stated otherwise, $\nabla R(\mathbf{x})$ is computed using automatic differentiation.

2.1 Fields-of-Experts Regularizer

In [55, 56], the authors discuss learning specific instances of the **fields of experts (FoE)** [130], which takes the general form

$$R(\mathbf{x}) = \sum_{j=1}^c \langle \mathbf{1}, \psi_j(\mathbf{W}_j \mathbf{x}) \rangle. \quad (6)$$

For each of the c filters, the potentials $\psi_j: \mathbb{R} \rightarrow \mathbb{R}^+$ are applied componentwise and $\mathbf{W}_j: \mathbb{R}^d \rightarrow \mathbb{R}^d$ are convolutions. Hence, R is a spatial penalization of multiple filter responses. Choosing $c = 2$, $\mathbf{W}_1 = \mathbf{D}_x$, $\mathbf{W}_2 = \mathbf{D}_y$ and $\psi_1 = \psi_2 = |\cdot|$ leads to the **TV** regularizer [131], which often serves as a baseline. If $\psi_j \in C^1(\mathbb{R})$, then

$$\nabla R(\mathbf{x}) = \sum_{j=1}^c \mathbf{W}_j^T \psi'_j(\mathbf{W}_j \mathbf{x}). \quad (7)$$

In Figure 1, we visualize a specification of the **FoE** with learned ψ_j and \mathbf{W}_j .

The authors of [55, 56] parameterize the $(\mathbf{W}_j)_{j=1}^c$ as a multi-convolution (an instance of linear neural networks [14, 18]). More precisely, to efficiently explore a large field of view, they decompose $(\mathbf{W}_j)_{j=1}^c$ into a composition of zero-padded convolutions with kernels of size $k \times k$ and with an increasing number of output channels. The kernels of the first layer have zero mean. Moreover, $\|(\mathbf{W}_j)_{j=1}^c\|_2 = 1$ is required to avoid scaling ambiguities. This constraint is implemented via spectral normalization based on power iterations. An efficient estimation in terms of the discrete Fourier transform is given in [56].

The authors of [56] parameterize ψ_j as $\psi_j(x) = 1/\alpha_j^2 \psi^\beta(\alpha_j x)$, where the learnable $\alpha_j \in \mathbb{R}$ adapt a shared potential ψ^β . Here, the division by α_j^2 ensures that the maximum of the (weak) derivative ψ_j'' is independent of α_j . Using a shared profile makes R more interpretable and easier to analyze. In

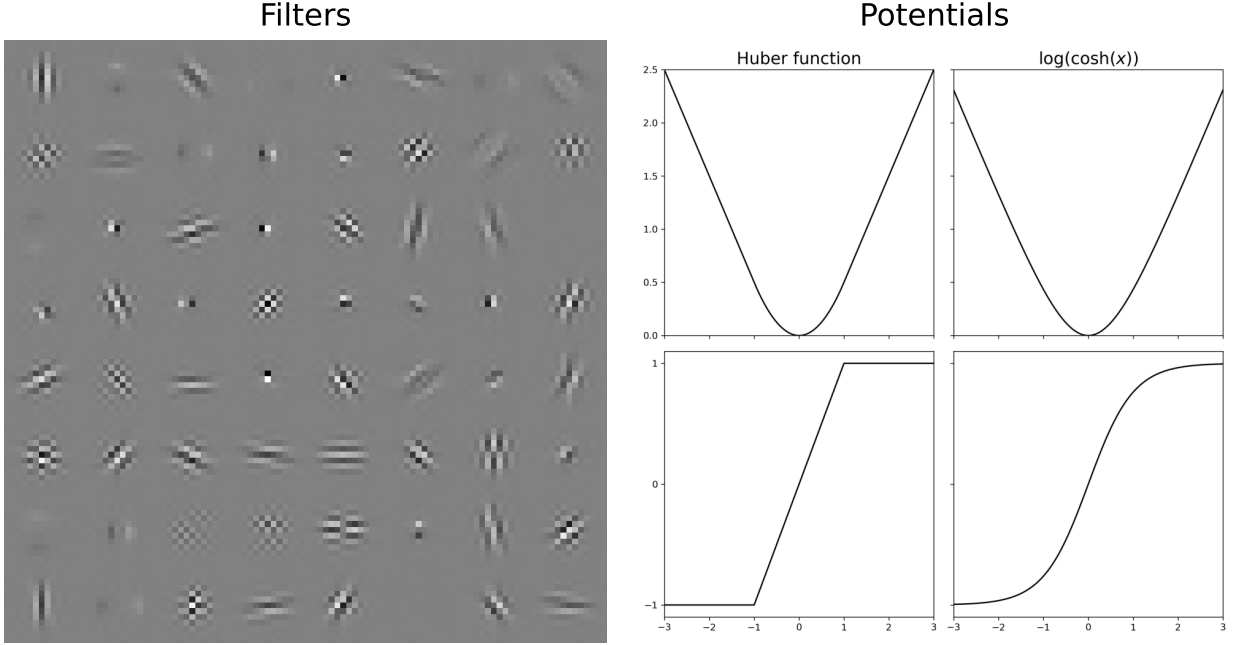


Figure 1: Left: The 64 filter impulse responses of a learned ridge regularizer. Right: The two discussed potentials ψ^1 and their derivative $\varphi^1 = (\psi^1)'$.

particular, if ψ^β is convex—which is the case when $(\psi^\beta)'' \geq 0$ a.e.—then R is convex which in turn guarantees that the objective function in (2) is convex. In contrast to [55, 56], which use learnable splines [45] to parameterize ψ^β , we simply use the Huber function (Moreau envelope of the ℓ_1 norm)

$$\psi^\beta(x) = \begin{cases} |x| - \frac{\beta^{-1}}{2} & |x| > \beta^{-1}, \\ \frac{\beta}{2}x^2 & |x| \leq \beta^{-1} \end{cases} \quad (8)$$

with a learnable parameter β . To ensure that $R \in C^\infty(\mathbb{R}^d)$, we can deploy $\psi^\beta(x) = \beta^{-1} \log(\cosh(\beta x))$ instead. By computing the derivatives, we directly verify that both options lead to a convex R . In the denoising case where $\mathbf{H} = \mathbf{I}$, the objective in (2) remains convex even if $(\psi^\beta)'' \geq -1$ a.e., that is, if ψ^β is 1-weakly convex. In this setting, we instead use $\tilde{\psi}^\beta(x) = \psi^\beta(x) - \psi^1(x)$ with $\beta \geq 0$ and one of the ψ^β from above. In accordance with [55, 56], we refer to these two instances of the [FoE](#) model as [CRR](#) and [WCRR](#), respectively. The overall set of parameters θ is given by the convolutions kernels W_j and the parameters of the potentials ψ_j for $j = 1, \dots, c$.

One possibility to make the architecture (6) more flexible is spatial adaptivity, namely to replace the constant vector $\mathbf{1}$ by spatially varying weights $\mathbf{\Lambda}_j$. These can be derived from the data \mathbf{y} as done in [105, 106, 120, 121]. Finally, a theoretical analysis for regularizers of the form (6) is performed in [105].

2.2 Convolutional Neural Network

Often, the starting point for constructing a learnable regularizer $R \in C^1(\mathbb{R}^d)$ is a [CNN](#). Here, $R = \mathbf{z}_\ell$, where \mathbf{z}_ℓ is defined recursively via

$$\mathbf{z}_1 = \psi_0(\mathbf{V}_0 \mathbf{x} + \mathbf{b}_0), \quad \mathbf{z}_{i+1} = \psi_i(\mathbf{W}_i \mathbf{z}_i + \mathbf{V}_i \mathbf{x} + \mathbf{b}_i), \quad i = 1, \dots, \ell - 1, \quad (9)$$

with parameters $\theta = \{(\mathbf{W}_i)_{i=1}^{\ell-1}, (\mathbf{V}_i)_{i=0}^{\ell-1}, (\mathbf{b}_i)_{i=0}^{\ell-1}\}$ and componentwise non-linear activation functions $\psi_i \in C^1(\mathbb{R})$. The operators \mathbf{W}_i , \mathbf{V}_i denote standard (linear) transformations such as convolutional or (averaged) pooling layers. Since \mathbf{z}_ℓ must be scalar, the output dimension of $\mathbf{W}_{\ell-1}$ and $\mathbf{V}_{\ell-1}$ must be one. Typical examples for ψ_i include

- the softplus $x \mapsto \log(1 + \exp(x))$;
- the hyperbolic tangent $x \mapsto \tanh(x) = \frac{\exp(x) - \exp(-x)}{\exp(x) + \exp(-x)}$;
- the sigmoid $x \mapsto 1/(1 + \exp(-x))$;
- the non-differentiable **rectified linear unit (ReLU)** $x \mapsto \max(x, 0)$ can be approximated by the smoothed (Moreau envelope) surrogate

$$\psi^\beta(x) = \begin{cases} 0 & \text{if } x \leq 0, \\ \frac{\beta}{2}x^2 & \text{if } 0 < x < \beta^{-1}, \\ x - \frac{\beta^{-1}}{2} & \text{otherwise.} \end{cases} \quad (10)$$

The **FoE** (6) is an instance of (9) with one hidden layer. In the next sections, we discuss more complex choices. The multi-scale architectures that we discuss in Sections 2.6 and 2.7 also include skip connections into (9).

2.3 Input Convex Neural Network

Several approaches to learning both convex as well as nonconvex R are based on **input-convex neural networks (ICNNs)** [6]. There, we constrain the \mathbf{W}_i and ψ_i such that (9) is a convex functional. For this, we use the fact that convexity is preserved under non-negative linear combinations and composition with a convex non-decreasing function. Thus, (9) is convex if the ψ_i are convex and non-decreasing, and the \mathbf{W}_i have non-negative entries. The activation functions ψ from Section 2.2 satisfy these properties. In [6], the non-negativity of the \mathbf{W}_i is enforced via zero clipping, i.e., by projecting the entries to the non-negative numbers after every training step. An alternative is to use positive parameterizations of the weights, for example via the exponential function.

For our experiments, we use an **ICNN** with two layers and no skip connections, namely

$$R(\mathbf{x}) = \sum_{j=1}^c a_j \langle \mathbf{1}, \psi_j(\mathbf{W}_{2,j} \mathbf{z}_j) \rangle, \quad \text{with } \mathbf{z}_j = \psi_j(\mathbf{W}_{1,j} \mathbf{x}). \quad (11)$$

In this model, the $\mathbf{W}_{i,j}$ as well as the coefficients a_j are learnable. The ψ_j are chosen as the smoothed **ReLU** with learnable β . More layers were difficult to train and did not lead to significant improvements in our experiments.

The idea of using **ICNNs** as regularizers goes back to [101]. Beyond this, **ICNNs** can be used to model R as the difference of convex functions [37, 160], see Section 2.4. Moreover, they enable strategies for learning a proximal operator, see Section 2.8. Another extension are weakly-convex **ICNNs** [138].

2.4 Input Difference-of-Convex Neural Network

While convexity of R leads to a convex objective in (2), it limits the expressiveness of R . One possibility for architectures with structured nonconvexity and thus more modeling flexibility is the **difference-of-convex (DC)** functions framework [37, 160]. There, R is written as

$$R(\mathbf{x}) = R_1(\mathbf{x}) - R_2(\mathbf{x}), \quad (12)$$

where R_1 and R_2 are convex. In this case, we say that R is a **DC** function. Several popular nonconvex, hand-crafted sparsity penalties fall in this class, including SCAD [49], MCP [156], the logarithmic

penalty [96], and the difference between the ℓ_1 -norm and ℓ_2 -norm [152]. The class of **DC** functions is broad and includes special classes of nonconvex functions, such as weakly-convex functions. Moreover, this class is closed under natural operations, such as linear combinations, multiplication, and division [88]. To learn a **DC** regularizer R , one can take R as the difference of two **ICNNs** R_1 and R_2 , see Section 2.3. We refer to this as an **input difference-of-convex neural network (IDCNN)**.

Due to the **DC** structure, we could leverage specialized algorithms when solving the corresponding variational problem (2). In particular, when the data fidelity $\mathbf{x} \mapsto D(\mathbf{Hx}, \mathbf{y})$ is convex, we can write the objective as the difference of $F_1(\mathbf{x}) := D(\mathbf{Hx}, \mathbf{y}) + \alpha R_1(\mathbf{x})$ and $F_2(\mathbf{x}) := \alpha R_2(\mathbf{x})$. Then, we can use the **DC** algorithm [88]. At each step, this algorithm linearizes the concave part $-F_2(\mathbf{x})$ and minimizes the resulting convex majorization of $F_1 - F_2$.

2.5 Patch-Based Architectures

Many priors are constructed such that they only use local information in images. Patch-based methods [116] exploit this idea by splitting the input into small regions of size $l \times l$, which we call patches. Well-known denoising algorithms based on this principle are non-local means [30] and BM3D [38]. Here, we consider patch-based regularizers R , namely the **expected patch log-likelihood (EPLL)** [162], **patch normalizing flow regularizer (PatchNR)** [5], and **local adversarial regularization (LAR)** [122]. A similar approach based on diffusion models was proposed in [73]. Formally, we define the patch extractor $E_i: \mathbb{R}^d \rightarrow \mathbb{R}^k$ with $k = l^2$ and $i = 1, \dots, s$, which extracts the i -th patch from the input image. Then, we define the regularizer R_θ as

$$R_\theta(\mathbf{x}) = \frac{1}{s} \sum_{i=1}^s r_\theta(E_i \mathbf{x}), \quad (13)$$

where $r_\theta: \mathbb{R}^k \rightarrow \mathbb{R}$ is a (learnable) regularizer on patches. Since every image contains a large number of patches, r_θ can be trained on very small datasets.

Both **EPLL** and **PatchNR** rely on statistical models to design r_θ . More precisely, we define $r_\theta(x) := -\log p_\theta(x)$, where p_θ is a distribution on the space of patches. The latter is usually learned using **patch-based maximum likelihood (PatchML)** estimation. **EPLL** typically models p_θ as a **Gaussian mixture model (GMM)** with c components, giving

$$\log p_\theta(x) = \log \left(\sum_{i=1}^c a_i g(x; \mu_i, \Sigma_i) \right), \quad (14)$$

where $g(x; \mu_i, \Sigma_i)$ is the multivariate Gaussian density with weights, means, and covariances $\theta = \{(a_i, \mu_i, \Sigma_i)\}_{i=1}^c$.

Instead, p_θ can be chosen as, e.g., constrained or generalized **GMMs** [41, 72, 107], distributions incorporating multi-scale [112] or sparsity elements [140]. Traditionally, the variational problem (2) is solved via half-quadratic splitting, which alternates between updates over the patches and the entire image. This involves several approximations, which introduces additional regularization.

PatchNR leverages **normalizing flows (NFS)** to parameterize p_θ . More precisely, given some latent distribution \mathbb{P}_Z (typically $z \sim \mathcal{N}(0, \mathbf{I})$) and a diffeomorphism $T_\theta: \mathbb{R}^k \rightarrow \mathbb{R}^k$, we define \mathbb{P}_θ via the push forward operator as $\mathbb{P}_\theta = (T_\theta)_\# \mathbb{P}_Z$. Its density can be calculated as

$$p_\theta(x) = p_z(T_\theta^{-1}(x)) |\det J_{T_\theta^{-1}}(x)|, \quad (15)$$

where $J_{T_\theta^{-1}}$ denotes the Jacobian of T_θ^{-1} . Evaluating p_θ requires an efficient inverse T_θ^{-1} and a tractable Jacobian determinant. To this end, T_θ is commonly implemented as invertible neural network with

affine coupling layers [43], where the input $\mathbf{x} \in \mathbb{R}^k$ is split into two parts as $\mathbf{x} = [\mathbf{x}_1, \mathbf{x}_2] \in \mathbb{R}^{k_1+k_2}$ and T_θ and T_θ^{-1} are defined as

$$\begin{array}{ll} \text{Forward Pass} & \text{Inverse Pass} \\ \mathbf{z}_1 = \mathbf{x}_1 & \Leftrightarrow \mathbf{x}_1 = \mathbf{z}_1 \\ \mathbf{z}_2 = \mathbf{x}_2 \odot \exp(s(\mathbf{x}_1)) + t(\mathbf{x}_1) & \mathbf{x}_2 = (\mathbf{z}_2 - t(\mathbf{z}_1)) \odot \exp(-s(\mathbf{z}_1)), \end{array} \quad (16)$$

where $s: \mathbb{R}^{k_1} \rightarrow \mathbb{R}^{k_2}$ and $t: \mathbb{R}^{k_1} \rightarrow \mathbb{R}^{k_2}$ are arbitrary (unconstrained) neural networks. Coupling layers are typically stacked alternatingly, i.e., components left unchanged in one layer are updated in the next.

Finally, we can define r_θ in (13) by a padding-free CNN, see [122]. Due to the valid padding the CNN takes an input patch of size $l \times l$ and returns a single number as an output. Consequently, the patch size l corresponds to the receptive field of the CNN determined by the kernel size and the number of layers. If we apply the same CNN to a larger image, the output corresponds to a matrix with the output of r_θ for all patches in the image. Hence, computing R_θ can be evaluated by applying the CNN and averaging over the outputs. The authors of [122] propose to learn such CNNs with LAR training, but most of the other training methods of Section 3 can be applied as well.

Many patch-based methods (including EPLL, PatchNR and padding-free CNNs) are prone to boundary artifacts since pixels at the image boundary are covered from fewer patches than interior pixels. As a remedy, we pad the input image in (13) by $l - 1$ pixels, where l is the patch size.

2.6 Total Deep Variation

In analogy to the FoE (6), total deep variation (TDV) [82] extends the model by incorporating a non-linear, multi-scale feature transform based on a CNN. For $\mathbf{x} \in \mathbb{R}^d$, TDV is defined as

$$R_{\text{TDV}}(\mathbf{x}) = \langle \mathbf{1}, \psi(\mathbf{w}\Psi(\mathbf{W}\mathbf{x})) \rangle, \quad (17)$$

where $\mathbf{W} \in \mathbb{R}^{dc \times d}$ is composed of c convolutions, $\Psi: \mathbb{R}^{dc} \rightarrow \mathbb{R}^{dc}$ is a multi-scale CNN, $\mathbf{w} \in \mathbb{R}^{d \times dc}$ is a 1×1 convolution, and $\psi: \mathbb{R} \rightarrow \mathbb{R}$ is a component-wise potential such as $\psi(x) = \frac{1}{2}x^2$ or $\psi(x) = \log(\cosh(x))$. Compared to other deep network-based regularizers, see for example [37, 163], the architecture (17) increases and reduces the channel number through \mathbf{W} and \mathbf{w} , respectively.

The computational structure of Ψ follows a hierarchical design and is visualized in Figure 2. Specifically, Ψ is composed of b sequential UNet type [129] macro-blocks $\text{Bl}^i, i \in \{1, \dots, b\}$ with a scales. We denote this as TDV_a^b . On each scale of Bl^i , we apply the residual micro-blocks

$$h_{j,k}^i(\mathbf{x}) = \mathbf{x} + \mathbf{W}_{j,k,2}^i \phi(\mathbf{W}_{j,k,1}^i \mathbf{x}), \quad j \in \{1, \dots, a\}, k \in \{1, 2\}, \quad (18)$$

where $\mathbf{W}_{j,k,1}^i, \mathbf{W}_{j,k,2}^i \in \mathbb{R}^{dc \times dc}$ are convolutions and $\phi: \mathbb{R} \rightarrow \mathbb{R}$ is a component-wise activation function.

While [82, 83] originally used Student-t type activation functions, we apply the softplus function for more stable training dynamics. The downsampling and upsampling operations within Ψ are implemented by strided 3×3 convolutions and transposed convolutions, respectively, combined with an anti-aliasing blur kernel, following [158]. Instead of symmetric boundary handling as in [82], we use zero boundary without a performance decrease.

Compared to the FoE (6), the TDV (17) uses a *non-linear* feature transform Ψ prior to the application of the potential ψ . Its hierarchical multi-scale architecture enables the extraction of more complex features over large spatial neighborhoods. Based on a mean-field control interpretation, robustness and stability results with respect to perturbations in both measurements and parameters were derived [83]. Successful applications of the TDV include accelerated MRI [104], structured illumination microscopy [149], exit wave reconstruction in transmission electron microscopy [117], and learning of binary sampling patterns for single-pixel imaging [144]. In combination with a patch-wise Wasserstein distance, TDV can also be used in unsupervised settings [118].

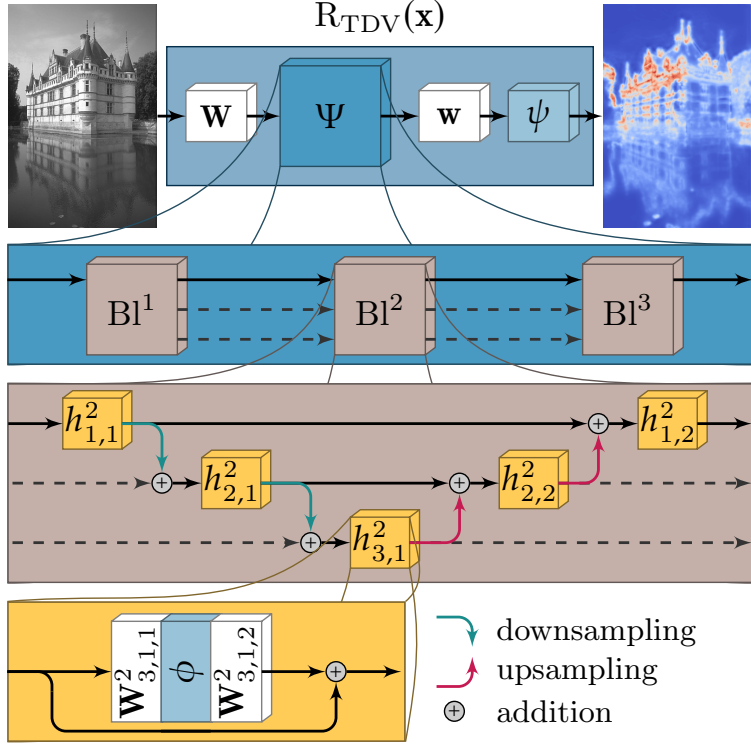


Figure 2: Visualization of TDV_3^3 . On the highest level, an energy value is assigned to every pixel by applying a CNN Ψ (blue). The CNN Ψ is composed of three UNet-like macro-blocks (gray). Each macro-blocks consists of five micro-blocks (yellow) with residual connections.

2.7 Least Squares Residual Regularizer

A common principle is that reconstructions live in a set (or manifold) \mathcal{M} , which can be characterized as the fixed points of a mapping $U: \mathbb{R}^d \rightarrow \mathbb{R}^d$. Then, penalizing the residuals $\mathbf{x} - U(\mathbf{x})$ yields a regularizer

$$R(\mathbf{x}) = \frac{1}{2} \|\mathbf{x} - U(\mathbf{x})\|^2, \quad (19)$$

which we refer to as the **least-squares residual (LSR)** regularizer. The minimum of (19) is attained when $U(\mathbf{x}) = \mathbf{x}$, that is, when \mathbf{x} is a fixed point. Further, its gradient is given by

$$\nabla R(\mathbf{x}) = (\mathbf{I} - J_U(\mathbf{x}))^T(\mathbf{x} - U(\mathbf{x})), \quad (20)$$

where the matrix-vector product with $J_U^T(\mathbf{x})$ can be computed using backpropagation. Typically, U is realized as an encoder-decoder architecture $U = D \circ E$, for example a UNet [129] or DRUNet [157]. Such networks are commonly initialized as pretrained image denoising or restoration networks [163].

LSR has been used for denoising [25], sparse-view CT [91], and, in combination with unrolling, for MRI reconstruction [2]. More recently, it has been used in the context of convergent PnP [37, 74] as gradient-step denoiser, and in [163] using bilevel training. In [109], the regularizer (19) is extended by an additional regularization within the fixed-point set of U .

2.8 Learned Proximal Networks

In the PnP framework, the proximal operator prox_R is learned from data. To this end, we need to parameterize prox_R , and ensure that the resulting operator is a prox. **Learned proximal networks (LPNs)** [50] provide a solution that allows evaluating the underlying R even though it is parameterized

implicitly. Based on the observation that gradients of convex functions fully characterize proximal operators [58], we define the reconstructor $\Psi_\theta: \mathbb{R}^d \rightarrow \mathbb{R}^d$ as

$$\Psi_\theta(\mathbf{x}) = \text{prox}_R(\mathbf{y}) = \nabla \Phi_\theta(\mathbf{x}), \quad (21)$$

where $\Phi_\theta \in C^1(\mathbb{R}^d)$ is a strongly convex potential with learnable parameters θ . Importantly, **LPNs** can provide proximals of *nonconvex* regularizers R since R is convex if and only if Φ_θ is 1-Lipschitz continuous (see [100, 58]), which is not required in **LPNs**. The value $R(\mathbf{x})$ for some $\mathbf{x} \in \mathbb{R}^d$ can be recovered via

$$R(\mathbf{x}) = \langle \Psi_\theta^{-1}(\mathbf{x}), \mathbf{x} \rangle - \frac{1}{2} \|\mathbf{x}\|_2^2 - \Phi_\theta(\Psi_\theta^{-1}(\mathbf{x})), \quad (22)$$

and its gradient reads $\nabla R(\mathbf{x}) = \Psi_\theta^{-1}(\mathbf{x}) - \mathbf{x}$. The inverse $\Psi_\theta^{-1}(\mathbf{x})$ satisfies

$$\Psi_\theta^{-1}(\mathbf{x}) = \arg \min_{\mathbf{v} \in \mathbb{R}^d} \{\Phi_\theta(\mathbf{v}) - \langle \mathbf{x}, \mathbf{v} \rangle\}, \quad (23)$$

allowing for its efficient computation by minimizing this strongly convex objective with the conjugate gradient method.

Typically, **LPNs** are trained on patches of size $l \times l$. When applying them to images \mathbf{x} of larger size $d = N \times N$, a classical approach is to employ a sliding window method with stride s satisfying $l \bmod s = 0$. To ensure that this results in a proximal operator, special care is necessary. We first zero-pad \mathbf{x} on one side of each dimension by $(s - (N \bmod s)) \bmod s$ entries and then add another $l - s$ zeros at both sides. As a result, all pixels of \mathbf{x} are covered by $(l/s)^2$ of the patches when sliding over the padded image $\tilde{\mathbf{x}}$. Denoting this (linear) padding process by \mathbf{P} , the resulting patch-based **LPN** reads

$$\tilde{\Psi}_\theta(\mathbf{x}) = \frac{s^2}{l^2} \mathbf{P}^T \sum_i E_i^T \Psi_\theta(E_i(\mathbf{P}\mathbf{x})), \quad (24)$$

which is the gradient of the convex function $\tilde{\Phi}_\theta(\mathbf{x}) = \frac{s^2}{l^2} \sum_i \Phi_\theta(E_i(\mathbf{P}\mathbf{x}))$ and thus again a proximal operator.

In practice, we realize the potential Φ_θ by an **ICNN** with softplus activation (see Section 2.3) and add a small quadratic term to make it strongly convex. The **ICNN** is based on the **CNN** architecture (9) and is more complex than the configuration described in Section 2.3. We initialize θ by taking the exponential of a Gaussian random variable to ensure non-negative values at initialization, which empirically improved the training speed.

Learning proximal or maximally monotone operators for deriving convergent **PnP** algorithms has been previously explored in [65, 70, 74, 115] and also the idea of employing gradient-based architectures in the context of **PnP** is not specific to **LPNs**. In particular, also the so-called *gradient-step* denoisers [37, 74] are designed as gradients of a potential Φ_θ . The work [75] makes use of the results in [108] to note that gradient-step denoisers induce a proximal operator whenever $\nabla \Phi_\theta$ is 1-Lipschitz. Since this is hard to enforce, a relaxation is used in implementations. Other works have explored weakly-convex regularizers R [56, 138], for which prox_R is well-defined. However, these explicit architectures for R do not provide closed-form evaluation for prox_R .

3 Overview of Training Methods

After choosing a parametric regularizer R_θ , the challenge lies in finding suitable parameters θ . In Table 2, we summarize the training methods included in our comparison. They mainly differ in how they incorporate training data and whether they make use of the operator \mathbf{H} . We classify the methods into supervised, semi-supervised or unsupervised as follows. Supervised methods can include

Table 2: Overview of Training Methods.

Data	Approach	Physics Description
supervised	Bilevel Learning (BL-IFT, BL-JFB, MAID)	✓/✗
semi-supervised	network Tikhonov (NETT)	✓/✗
	adversarial regularization (AR)	✓/✗
unsupervised	score matching (SM)	✗
	patch-based maximum likelihood (PatchML)	✗
	proximal matching (PM)	✗

the operator \mathbf{H} and use paired data of ideal images and corrupted data. Semi-supervised data may also use \mathbf{H} but do not rely on paired data. Unsupervised methods will not use \mathbf{H} nor any data related to the inverse problem of interest. Some methods can naturally be applied in multiple regimes.

For many approaches, suitable parameters can be found independently of \mathbf{H} , allowing deployment to any inverse problem after training. Regardless of the chosen training method, we deploy R_θ within the variational objective (2) during evaluation. This may require a further tuning of e.g., the regularization parameter α . Details on the minimization of (2) are given in Section 4.1.

3.1 Bilevel Learning

Given paired training data $(\mathbf{x}_i, \mathbf{y}_i) \in \mathbb{R}^d \times \mathbb{R}^m$, $i = 1, \dots, n$, supervised bilevel learning considers the nested optimization problem

$$\min_{\theta} \left\{ L(\theta) = \frac{1}{n} \sum_{i=1}^n G_{\mathbf{x}_i}(\hat{\mathbf{x}}_{\mathbf{y}_i}(\theta)) \right\} \text{ subject to } \quad (25)$$

$$\hat{\mathbf{x}}_{\mathbf{y}_i}(\theta) = \arg \min_{\mathbf{x}} \{ E_{\mathbf{y}_i}(\mathbf{x}; \theta) = D(\mathbf{H}\mathbf{x}, \mathbf{y}_i) + \alpha R_\theta(\mathbf{x}) \}, \quad (26)$$

where L assesses θ by comparing the reconstruction $\hat{\mathbf{x}}_{\mathbf{y}_i}(\theta)$ to the ground truth image \mathbf{x}_i via the function $G_{\mathbf{x}_i}$. The reconstruction $\hat{\mathbf{x}}_{\mathbf{y}_i}(\theta)$ is connected to R_θ via the lower-level problem (26).

Minimization and Hypergradients Most bilevel solvers rely on gradient-based optimization. In the learning context, one often uses stochastic variants such as [Adaptive Moment Estimation optimizer \(Adam\)](#) [81], which use only a random subset of the training data $(\mathbf{x}_i, \mathbf{y}_i)$ for every update of θ . This requires the (stochastic) gradient of L with respect to θ , which is often referred to as hypergradient. We now review various ways to compute this gradient. For notational simplicity, we set $n = 1$ in the following. Using the chain rule, we obtain

$$\nabla_{\theta} L(\theta) = [D_{\theta} \hat{\mathbf{x}}_{\mathbf{y}_i}(\theta)]^T \nabla_{\mathbf{x}} G_{\mathbf{x}_i}(\hat{\mathbf{x}}_{\mathbf{y}_i}(\theta)), \quad (27)$$

where $D_{\theta} \hat{\mathbf{x}}_{\mathbf{y}_i}(\theta)$ is the derivative of $\theta \mapsto \hat{\mathbf{x}}_{\mathbf{y}_i}(\theta)$. The main challenge of (27) is the computation of $D_{\theta} \hat{\mathbf{x}}_{\mathbf{y}_i}(\theta)$. A comparison and detailed discussion of approaches can be found in [16, 78, 92, 164]. We now briefly discuss four popular options.

3.1.1 Implicit Differentiation

The [BL-IFT](#) [22, 57, 134] approach involves implicitly differentiating the optimality condition of (26), which reads

$$\nabla_{\mathbf{x}} E_{\mathbf{y}_i}(\hat{\mathbf{x}}_{\mathbf{y}_i}(\theta); \theta) = 0. \quad (28)$$

Given θ , we compute $\hat{\mathbf{x}}_{\mathbf{y}_i}(\theta)$ as described in Section 4.1 (also known as forward solve). If $E_{\mathbf{y}_i}(\cdot; \theta) \in C^2(\mathbb{R}^d)$ and its Hessian $\mathbf{S}(\theta) = \nabla_{\mathbf{x}}^2 E_{\mathbf{y}_i}(\hat{\mathbf{x}}_{\mathbf{y}_i}(\theta); \theta)$ is invertible for a given θ , then the [implicit function theorem \(IFT\)](#) guarantees the existence of a continuously differentiable solution map $\theta \mapsto \hat{\mathbf{x}}_{\mathbf{y}_i}(\theta)$ locally. The invertibility condition is for example satisfied if $E_{\mathbf{y}_i}(\cdot; \theta)$ is strictly convex or if $\hat{\mathbf{x}}_{\mathbf{y}_i}(\theta)$ is a nondegenerate local minimum. Differentiating (28) with respect to θ leads to

$$0 = \mathbf{S}(\theta) D_{\theta} \hat{\mathbf{x}}_{\mathbf{y}_i}(\theta) + \mathbf{J}(\theta) \quad (29)$$

with $\mathbf{J}(\theta)$ given by the Jacobian of $\theta \mapsto \nabla_{\mathbf{x}} E_{\mathbf{y}_i}(\hat{\mathbf{x}}_{\mathbf{y}_i}(\theta); \theta)$, that is $\mathbf{J}(\theta) = \nabla_{\theta, \mathbf{x}} E_{\mathbf{y}_i}(\hat{\mathbf{x}}_{\mathbf{y}_i}(\theta); \theta)$. Thus, the hypergradient (27) is formally given by

$$\nabla_{\theta} L(\theta) = -[\mathbf{J}(\theta)]^T [\mathbf{S}(\theta)]^{-1} \nabla_{\mathbf{x}} G_{\mathbf{x}_i}(\hat{\mathbf{x}}_{\mathbf{y}_i}(\theta)). \quad (30)$$

In practice, we compute the solution $\hat{\mathbf{x}}_{\mathbf{y}_i}(\theta)$ of (26) numerically and replace the inversion of the Hessian in (30) by solving the linear system (29) for $\hat{\mathbf{x}}_{\mathbf{y}_i}(\theta)$ with an iterative algorithm (such as [conjugate gradient method \(CG\)](#) or [minimal residual method \(MINRES\)](#)). Assuming that both steps are exact and that the Hessian $\mathbf{S}(\theta)$ is invertible, (30) can be computed exactly. However, iterative solvers only compute an approximation, so the accuracy for both solvers has to be carefully selected. The computational complexity and memory requirements for solving (29) are independent of the solver specifications for the lower-level problem (26). In particular, we do not have to trace its computational path. However, solving the linear system (29) requires evaluating many Hessian-vector products, the number of which depends on the system's conditioning. When computed via automatic differentiation, each iteration can become expensive, especially for R_{θ} with large architectures.

Recent work has extended the [IFT](#) to merely Lipschitz continuous lower-level problems [26], which is particularly relevant in practice since many approaches employ non-smooth activation functions such as [ReLU](#) in R_{θ} .

3.1.2 Unrolling

Recall that we compute $\hat{\mathbf{x}}_{\mathbf{y}_i}(\theta)$ with an iterative forward solver of the form

$$\mathbf{x}^{(k+1)} = T(\mathbf{x}^{(k)}; \theta), \text{ for } k = 0, 1, \dots, k_u - 1, \quad (31)$$

where k_u is the fixed number of iterations, $\mathbf{x}^{(0)}$ is some starting guess and $T(\cdot; \theta)$ is defined such that solutions of (28) are fixed points of $T(\cdot; \theta)$. To simplify our considerations, we only discuss the gradient descent step $T(\mathbf{x}; \theta) = \mathbf{x} - \tau \nabla_{\mathbf{x}} E_{\mathbf{y}_i}(\mathbf{x}; \theta)$, where the step size τ is added to the learnable parameters θ . More sophisticated routines with momentum, such as the evaluation routine from Section 4.1, can be used instead. In contrast to the [BL-IFT](#) approach, we compute $D_{\theta} \hat{\mathbf{x}}_{\mathbf{y}_i}(\theta)$ by applying the chain rule to (31), which leads to

$$D_{\theta} \hat{\mathbf{x}}_{\mathbf{y}_i}(\theta) \approx D_{\theta} \mathbf{x}^{(k_u)} = \sum_{k=1}^{k_u} \mathbf{A}_{k_u} \dots \mathbf{A}_{k+1} \mathbf{B}_k, \text{ where} \\ \mathbf{A}_{k+1} = D_{\mathbf{x}} T(\mathbf{x}^{(k)}; \theta), \text{ and } \mathbf{B}_{k+1} = D_{\theta} T(\mathbf{x}^{(k)}; \theta). \quad (32)$$

This approach is commonly known as unrolling [97, 110] and corresponds to the *exact* gradient of the finite iterative scheme (31). An overview of unrolling is provided in [99], and a more general perspective based on the *learning-to-optimize* framework is given in [34]. The expression (32) can be efficiently evaluated using backpropagation, which requires storing the intermediate variables $\mathbf{x}^{(k)}$ for $k = 1, \dots, k_u$. Hence, the memory requirement of backpropagation through (31) grows linearly with k_u , which restricts the number of steps k_u that we can take. However, if k_u is small, (31) does not necessarily lead to a good approximation of a minimizer $\hat{\mathbf{x}}_{\mathbf{y}_i}(\theta)$ for (26). Still, unrolling has been used successfully together with an adaption of α in (2) for the [CRR](#) [55]. In principle, the memory usage can be decreased by checkpointing [59]. To stabilize the training, we can regularize $\nabla_{\mathbf{x}}^2 E_{\mathbf{y}_i}(\cdot; \theta)$ in (26) [17] or perform (31) with a random number of steps k_u and random initializations $\mathbf{x}^{(0)}$ [7].

3.1.3 Jacobian-free Backpropagation

A memory-efficient alternative to unrolling is **Jacobian-free backpropagation (JFB)** [27, 52] (also known as truncated backpropagation [136, 146]). Instead of backpropagating through the whole scheme (31), we only do so for the last k_b steps and approximate

$$D_\theta \mathbf{x}^{(k_u)} \approx \sum_{k=k_u-k_b+1}^{k_u} \mathbf{A}_{k_u} \dots \mathbf{A}_{k+1} \mathbf{B}_k. \quad (33)$$

Under certain regularity assumptions, the truncation error induced by (33) decays exponentially as k_b increases [136]. Moreover, the obtained hypergradient is a descent direction for (25) under reasonable assumptions [136]. Since checking the assumptions is infeasible, the results merely serve as motivation.

There is a direct relation to the **BL-IFT** approach. Let $\mathbf{A}_\infty = D_\mathbf{x} T(\hat{\mathbf{x}}_{\mathbf{y}_i}(\theta); \theta)$ with T from (31) and $\mathbf{B}_\infty = D_\theta T(\hat{\mathbf{x}}_{\mathbf{y}_i}(\theta); \theta)$. Then, close to the equilibrium $\hat{\mathbf{x}}_{\mathbf{y}_i}(\theta)$, we can approximate (33) with the Neumann series

$$D_\theta \hat{\mathbf{x}}_{\mathbf{y}_i}(\theta) \approx \left(\sum_{k=0}^{k_b-1} \mathbf{A}_\infty^k \right) \mathbf{B}_\infty, \quad (34)$$

which converges to $(\mathbf{I} - \mathbf{A}_\infty)^{-1} \mathbf{B}_\infty$ as $k_b \rightarrow \infty$ if $\|\mathbf{A}_\infty\|_2 < 1$. The formula (34) is known as Neumann backpropagation [92] and differs from (33) by using only the output $\hat{\mathbf{x}}_{\mathbf{y}_i}(\theta)$ instead of the last k_b steps of (31). For gradient descent, we have $\mathbf{A}_\infty = \mathbf{I} - \tau \nabla_{\mathbf{x}}^2 E_{\mathbf{y}_i}(\hat{\mathbf{x}}_{\mathbf{y}_i}(\theta); \theta)$. It holds $\|\mathbf{A}_\infty\|_2 < 1$ if τ is small enough and $\nabla_{\mathbf{x}}^2 E_{\mathbf{y}_i}(\hat{\mathbf{x}}_{\mathbf{y}_i}(\theta); \theta)$ is positive definite, namely if $\hat{\mathbf{x}}_{\mathbf{y}_i}(\theta)$ minimizes $E_{\mathbf{y}_i}(\cdot; \theta)$. In this case, (34) converges to the **IFT** gradient (30) as $k_b \rightarrow \infty$. A deeper study can be found in [92]. In practice, choosing $k_b = 1$ often works well [27, 52].

3.1.4 Adaptive Accuracy

Several works have analyzed the convergence of bilevel optimization based on the assumption that the hypergradients are computed with high accuracy [114]. Many of these approaches rely on line-search, which requires access to exact solutions of the lower-level problem (26). However, (26) is typically solved approximately using an iterative method. Hence, the inexact solution $\tilde{\mathbf{x}}_{\mathbf{y}}(\theta_k)$ and $D_\theta \tilde{\mathbf{x}}_{\mathbf{y}}(\theta_k)$ for the upper level problem (25) at iteration k might be too inaccurate for the **BL-IFT** theory to hold.

To address this, the **method of adaptive inexact descent (MAID)** [132] adaptively selects both the upper-level step size and the accuracy of the lower-level solver. This requires error bounds for the lower-level solutions and computable error bounds for the inexact hypergradients. At each upper-level iteration k , an approximate lower-level solution $\tilde{\mathbf{x}}_{\mathbf{y}}(\theta_k)$ satisfying $\|\tilde{\mathbf{x}}_{\mathbf{y}}(\theta_k) - \hat{\mathbf{x}}_{\mathbf{y}}(\theta_k)\| \leq \epsilon_k$ is computed for a given tolerance $\epsilon_k \geq 0$. Then, an approximation \mathbf{q}_k of $\mathbf{S}(\theta_k)^{-1} \nabla_{\mathbf{x}} G_{\mathbf{x}}(\tilde{\mathbf{x}}_{\mathbf{y}}(\theta_k))$ is computed by solving the corresponding linear system up to the tolerance $\delta_k \geq 0$. An approximate hypergradient \mathbf{z}_k that satisfies $\|\mathbf{z}_k - \nabla L(\theta_k)\| = \mathcal{O}(\epsilon_k + \delta_k)$ [48] is then given by

$$\mathbf{z}_k = -[\nabla_{\theta, \mathbf{x}} E_{\mathbf{y}_i}(\tilde{\mathbf{x}}_{\mathbf{y}_i}(\theta); \theta)]^T \mathbf{q}_k. \quad (35)$$

Motivated by Armijo-type line search, we define the following function for checking sufficient decrease

$$\xi(\alpha_k) := \Delta_{k+1}^+ - \Delta_k^- + \lambda \alpha_k \|\mathbf{z}_k\|^2, \quad (36)$$

where $\Delta_l^\pm := G_{\mathbf{x}}(\tilde{\mathbf{x}}_{\mathbf{y}}(\theta_l)) \pm (\|\nabla_{\mathbf{x}} G_{\mathbf{x}}(\tilde{\mathbf{x}}_{\mathbf{y}}(\theta_l))\| \epsilon_l + \frac{\gamma}{2} \epsilon_l^2)$ are upper and lower bounds on $L(\theta_l)$, respectively. Here, γ is the Lipschitz constant of $\nabla G_{\mathbf{x}}$. If $\xi(\alpha_k) \leq 0$ for some $\lambda > 0$ (e.g., $\lambda = 10^{-4}$), sufficient decrease in the objective (25) can be ensured [132, Lemma 3.5]. Otherwise, the accuracy or the step size is unsuitable and needs to be modified. The full scheme is given as Algorithm 1, and its convergence to a critical point is shown in [132, Thm. 3.19].

Algorithm 1 **MAID** to solve bilevel learning problem (25).

Hyperparameters: step size controls $0 < \underline{\rho} < 1 < \bar{\rho}$; accuracy controls $0 < \underline{\nu} < 1 < \bar{\nu}$; maximum backtracking iterations $b \in \mathbb{N}$.

```

1: Input:  $\theta_0$ , accuracies  $\epsilon_0, \delta_0 > 0$ , step size  $\alpha_0 > 0$ .
2: for  $k = 0, 1, \dots$  do
3:   for  $j = b, b + 1, \dots$  do
4:      $\mathbf{z}_k \leftarrow \text{inexact\_grad}(\theta_k, \epsilon_k, \delta_k)$  ▷ inexact hypergradient using (35)
5:     for  $i = 0, 1, \dots, j - 1$  do
6:       if  $\xi(\alpha_k) \leq 0$  then ▷ inexact sufficient decrease using (36)
7:          $\theta_{k+1} \leftarrow \theta_k - \alpha_k \mathbf{z}_k$  ▷ gradient descent update
8:         go to line 11 ▷ backtracking successful
9:        $\alpha_k \leftarrow \underline{\rho} \alpha_k$  ▷ decrease step size
10:       $\epsilon_k, \delta_k \leftarrow \underline{\nu} \epsilon_k, \underline{\nu} \delta_k$  ▷ backtracking failed; needs higher accuracy
11:       $\epsilon_{k+1}, \delta_{k+1}, \alpha_{k+1} \leftarrow \bar{\nu} \epsilon_k, \bar{\nu} \delta_k, \bar{\rho} \alpha_k$  ▷ increase parameters

```

The implemented **MAID** uses gradient descent as a starting point and introduces the inaccurate handling of gradients. Of course, this idea can be generalized to other algorithms. However, extensions to stochastic gradients are not straightforward due to its reliance on backtracking. A stochastic version with nonadaptive accuracy has been recently proposed [133].

3.2 Contrastive Learning

Bilevel learning aims to directly learn the reconstruction operator. Another class of methods tries to learn a regularizer R by contrasting “good” and “bad” images. This approach shares similarities with contrastive learning, which originates from representation learning [21, 35], and has been applied in various fields such as generative modeling [53] and latent space embeddings [123].

3.2.1 Network Tikhonov

The **network Tikhonov (NETT)** approach [8, 91, 109] learns a regularizer of the form $R = J \circ \Psi_\theta$, where $J: \mathbb{R}^d \rightarrow [0, \infty]$ is a “distance” functional and $\Psi_\theta: \mathbb{R}^d \rightarrow \mathbb{R}^d$ is a parametric network designed to extract artifacts. A typical choice for Ψ_θ is an encoder-decoder architecture $\Psi_\theta = D_\theta \circ E_\theta$, with $J(\cdot) = \|\cdot\|_2^2$, see also Section 2.7. In particular, Ψ_θ aims to model the residual between clean and degraded images, thereby modeling artifacts. Given a degradation operator $\mathbf{z} = G(\mathbf{x}, \mathbf{y})$, the training of Ψ_θ is designed to ensure the following: (i) when given a degraded image $G(\mathbf{x}, \mathbf{y})$ with corresponding ground truth \mathbf{x} , the network should output the artifacts, i.e., the difference $G(\mathbf{x}, \mathbf{y}) - \mathbf{x}$; and (ii) when given a clean image \mathbf{x} , the network should output zero. Examples of degradation operators are $G(\mathbf{x}, \mathbf{y}) = \mathbf{H}^\dagger(\mathbf{H}\mathbf{x} + \mathbf{n})$ when the noise model \mathbf{n} and the forward map are known, and $G(\mathbf{x}, \mathbf{y}) = \mathbf{H}^\dagger(\mathbf{y})$ when supervised training data are available. Both lead to penalization of artifacts introduced by the application of \mathbf{H}^\dagger if (1) is ill-posed. In any case, the R is trained such that it takes large values for degraded images $G(\mathbf{x}_i, \mathbf{y}_i)$, $i = 1, \dots, n$, and small values for clean images \mathbf{x}_j , $j = 1, \dots, m$. This can be achieved with the reconstruction loss

$$L(\theta) = \frac{1}{n} \sum_{i=1}^n \|G(\mathbf{x}_i, \mathbf{y}_i) - \mathbf{x}_i - \Psi_\theta(G(\mathbf{x}_i, \mathbf{y}_i))\|^2 + \frac{1}{m} \sum_{j=1}^m \|\Psi_\theta(\mathbf{x}_j)\|^2. \quad (37)$$

Note that the training does not involve the functional J . Once trained, the reconstruction is done by solving (2), where the regularization parameter α needs to be tuned. It is also possible to use multiple trained R to better capture unwanted structure (e.g., nullspace components or noise). Under

natural assumptions on J and Ψ , NETT leads to a convergent regularization method [91]. A related approach, non-stationary iterated network Tikhonov (iNETT) has been proposed and analyzed in [24]. The convergence of the iterated Tikhonov method can be guaranteed by incorporating uniformly convex networks.

3.2.2 Adversarial Regularization

Adversarial regularization (AR) [93, 101, 137, 138, 160] operates within a weakly supervised setting. There, we assume to be given desirable images \mathbf{x}_i , $i = 1, \dots, n$, and (noisy) measurements \mathbf{y}_j , $j = 1, \dots, \tilde{n}$, which originate from distributions \mathbb{P}_X and \mathbb{P}_Y , respectively. This semi-supervised setting is more realistic in applications where ground truth images are unavailable. To consider both distributions in the same space, we push-forward \mathbb{P}_Y from the measurement space \mathbb{R}^m to the image space \mathbb{R}^d using a (potentially regularized) pseudo-inverse \mathbf{H}^\dagger , giving a distribution $\mathbb{P}_{\mathbf{H}} := (\mathbf{H}^\dagger)_\# \mathbb{P}_Y$ of images with artifacts. The key idea of AR is to train R_θ as a classifier. More precisely, R_θ should be small on real samples from \mathbb{P}_X and large on the artificial ones from $\mathbb{P}_{\mathbf{H}}$. To achieve this, a natural training loss is

$$L(\theta) = \frac{1}{n} \sum_{i=1}^n R_\theta(\mathbf{x}_i) - \frac{1}{\tilde{n}} \sum_{j=1}^{\tilde{n}} R_\theta(\mathbf{H}^\dagger \mathbf{y}_j) + \lambda \mathbb{E}_{\mathbf{x}} [(\|\nabla R_\theta(\mathbf{x})\| - 1)_+^2], \quad (38)$$

where $x_+ = \max\{x, 0\}$. The last term serves as regularization that promotes the classifier R_θ to be 1-Lipschitz, inspired by the Wasserstein GAN (WGAN) loss [12], and the expectation is taken over points of the form

$$\mathbf{x} = t\mathbf{x}_i + (1-t)\mathbf{H}^\dagger \mathbf{y}_j, \quad (39)$$

where $\mathbf{x}_i \sim \mathbb{P}_X$, $\mathbf{y}_j \sim \mathbb{P}_Y$, and $t \sim \mathcal{U}[0, 1]$. A patch-based variant of the AR training was proposed in [122] under the name **local adversarial regularization (LAR)** in combination with padding-free CNNs, see Section 2.5. Here, we use a loss similar to (38) with patches extracted from both \mathbf{x}_i and $\mathbf{H}^\dagger \mathbf{y}_j$.

Utilizing (38) provides an interesting characterization of the optimal R_θ [93]. Let us assume that \mathbb{P}_X is supported on a compact set \mathcal{M} which captures the intuition that images lie in a lower-dimensional non-linear subspace of the original space, see also Section 3.2.1. Let $\text{proj}_{\mathcal{M}}$ denote the orthogonal projection onto \mathcal{M} . Further, we assume that \mathbb{P}_X and $\mathbb{P}_{\mathbf{H}}$ satisfy $(\text{proj}_{\mathcal{M}})_\# \mathbb{P}_{\mathbf{H}} = \mathbb{P}_X$. This means that the reconstruction artifacts are small enough to allow recovery of the real distribution by simply projecting samples from $\mathbb{P}_{\mathbf{H}}$ onto \mathcal{M} . Then, the distance function $\mathbf{x} \mapsto \min_{\mathbf{z} \in \mathcal{M}} \|\mathbf{x} - \mathbf{z}\|$ is a maximizer of

$$\mathbb{W}_1(\mathbb{P}_{\mathbf{H}}, \mathbb{P}_X) = \sup_{f \in 1\text{-Lip}} \mathbb{E}_{\mathbf{x} \sim \mathbb{P}_{\mathbf{H}}} [f(\mathbf{x})] - \mathbb{E}_{\mathbf{x} \sim \mathbb{P}_X} [f(\mathbf{x})], \quad (40)$$

which is the formal limit of (38) for $\lambda \rightarrow \infty$. For evaluation, we rescale R to ensure that $\|\nabla R(\mathbf{x})\| \leq 1$ on the validation set. Regarding the variational problem (2), we set $\alpha = \mathbb{E}_{\mathbf{n} \sim \mathbb{P}_N} \|\mathbf{H}^T \mathbf{n}\|_2$ provided that the noise distribution \mathbb{P}_N is known [93]. This initial estimate of α can be further refined if needed.

3.3 Distribution Matching

From the Bayesian viewpoint, the ground truth \mathbf{x} and the observation \mathbf{y} in the inverse problem (1) are samples from distributions p_X and p_Y . As outlined in Section 1, the solution of the variational problem (2) corresponds to the MAP estimator of X given $Y = \mathbf{y}$. In particular, R is given (up to a constant) by $R(\mathbf{x}) \propto -\log(p_X(\mathbf{x}))$ or, equivalently, p_X corresponds to the so-called Gibbs prior $p_X(\mathbf{x}) \propto \exp(-R(\mathbf{x}))$. Thus, one can estimate p_X to learn the parameters θ of R_θ . In contrast to all previous methods, the ones discussed here are independent of the operator \mathbf{H} , the noise model, and the data term D .

3.3.1 Maximum Likelihood Training

Let $p_\theta(\mathbf{x}) = Z_\theta^{-1} \exp(-R_\theta(\mathbf{x}))$ denote the Gibbs prior with normalizing constant $Z_\theta = \int_{\mathbb{R}^d} \exp(-R_\theta(\mathbf{x})) d\mathbf{x}$. Then, given training samples $\mathbf{x}_1, \dots, \mathbf{x}_n$ from p_X , the parameters θ can be learned by computing the maximum likelihood estimator

$$\theta_{\text{ML}} = \arg \max_{\theta} \left\{ \sum_{i=1}^n \log(p_\theta(\mathbf{x}_i)) \right\} = \arg \min_{\theta} \left\{ \sum_{i=1}^n R_\theta(\mathbf{x}_i) + \log(Z_\theta) \right\}. \quad (41)$$

The estimator (41) is an empirical estimator of the Kullback–Leibler divergence

$$(p_X \mid p_\theta)_{\text{KL}} = \mathbb{E}_{\mathbf{x} \sim p_X} \left[\log \left(\frac{p_X(\mathbf{x})}{p_\theta(\mathbf{x})} \right) \right]. \quad (42)$$

More precisely, by replacing the empirical sum by an expectation, we obtain that

$$\theta_{\text{ML}} \approx \arg \min_{\theta} \mathbb{E}_{\mathbf{x} \sim p_X} [-\log(p_\theta(\mathbf{x}))] = \arg \min_{\theta} (p_X \mid p_\theta)_{\text{KL}}. \quad (43)$$

The main difficulty in this approach is the computation of Z_θ . One possibility is to choose the architecture of R_θ such that $Z_\theta = 1$ is true independently of θ . This holds for the Gibbs prior of parametric distributions such as Gaussians [3] (which corresponds to the optimal Tikhonov regularizer), [GMMs](#) [162], [NFs](#) [5, 11, 42], or other generative models.

Unfortunately, such models are often not expressive enough to provide a meaningful approximation of p_X . Therefore, patch-based architectures like [EPLL](#) and [PatchNR](#) approximate the distribution of patches instead, see Section 2.5 for details. In this case, we use a [PatchML](#) objective

$$\arg \min_{\theta} \mathbb{E}_{\mathbf{x} \sim p_Q} [-\log p_\theta(\mathbf{x})], \quad (44)$$

where the distribution p_Q of $l \times l$ patches is induced by p_X [5, Lem. 3].

We can rewrite the gradient of the maximum likelihood loss in (42) as

$$\begin{aligned} \nabla_{\theta} \mathbb{E}_{\mathbf{x} \sim p_X} [-\log(p_\theta(\mathbf{x}))] &= \mathbb{E}_{\mathbf{x} \sim p_X} [\nabla_{\theta} R_\theta(\mathbf{x})] + \nabla_{\theta} \log(Z_\theta) \\ &= \mathbb{E}_{\mathbf{x} \sim p_X} [\nabla_{\theta} R_\theta(\mathbf{x})] - \mathbb{E}_{\mathbf{x} \sim p_\theta} [\nabla_{\theta} R_\theta(\mathbf{x})], \end{aligned} \quad (45)$$

see [71] for a detailed derivation of the second step. In the context of imaging, (45) was also studied under the name “difference-of-expectations objective” in [142, 153, 155]. Still, the computation of the second expectation in (45) requires sampling from p_θ . This is often realized via Monte Carlo sampling, which makes these methods computationally expensive [61, 86, 142]. The form (45) also links the maximum likelihood approach with the contrastive learning methods discussed in Section 3.2. There, p_θ is replaced by an “adversarial distribution” of degraded images.

3.3.2 Score Matching

An alternative to estimating p_X is to estimate its gradient $\nabla \log p_X$, which is also known as the Stein score. However, accessing $\nabla \log p_X$ directly is usually intractable. Instead, we consider the *noisy* random variable $X_\sigma = X + \sigma \eta$ with $\eta \sim \mathcal{N}(0, I)$. Then, the score $s_\sigma = \nabla \log p_\sigma$ with $p_\sigma := p_{X_\sigma}$ can be characterized by Tweedie’s formula [98, 47] as

$$s_\sigma = \arg \min_f \mathbb{E}_{\mathbf{x} \sim X, \mathbf{n} \sim \eta} [\|f(\mathbf{x} + \sigma \mathbf{n}) - \mathbf{n}\|^2]. \quad (46)$$

Consequently, we can learn the parameters θ such that R_θ approximates $\mathbf{x} \mapsto -\log p_\sigma(\mathbf{x})$ (up to a constant) by minimizing the [score matching \(SM\)](#) loss [76, 139] given by

$$\theta_{\text{SM}} = \arg \min_{\theta} \mathbb{E}_{\mathbf{x} \sim p_X, \mathbf{n} \sim \eta} [\|\nabla R_\theta(\mathbf{x} + \sigma \mathbf{n}) - \mathbf{n}\|^2]. \quad (47)$$

Similarly to (41), the **SM** loss in (47) can be interpreted as a divergence. More precisely, θ_{SM} minimize the Fisher divergence

$$(p_\sigma \mid p_\theta)_{\text{F}} = \int_{\mathbb{R}^d} p_\sigma(\mathbf{x}) \|\nabla \log p_\sigma(\mathbf{x}) - \nabla \log p_\theta(\mathbf{x})\|^2 d\mathbf{x}. \quad (48)$$

As an important consequence, we observe that the **SM** loss approximates p_σ instead of p_X , which introduces a bias that increases for larger σ . At the same time, if σ is chosen too small, the learned R_θ becomes imprecise in low-density areas of p_X since the influence of these areas vanishes in (48) as $\sigma \rightarrow 0$.

While the smoothing bias of p_σ often limits the effectiveness of R_θ learned by **SM**, the minimization of (47) is computationally efficient. Therefore, **SM** is used as a pretraining step for the bilevel routines described in Section 3.1, see also [163]. That is, we first compute the optimal parameters θ_{SM} for the loss (47), and then use θ_{SM} as an initialization in the bilevel problem (25).

3.3.3 Proximal Matching

Finally, we discuss an approach to approximate $-\log p_X$ implicitly via its proximal operator. The latter is parameterized by some network Ψ_θ . Such approaches are widely studied in the context of **PnP** methods [51, 70, 124, 145, 157]. Here, we solely consider the case where $\Psi_\theta = \text{prox}_{R_\theta}$ for some underlying R_θ . This is fulfilled, for instance, for the **LPNs** in Section 2.8. Another possibility is the gradient-step denoiser [37, 74] provided that the involved potential is 1-Lipschitz continuous (which is intractable to enforce in practice).

To approximate $\text{prox}_{-\sigma^2 \log p_X}$ with Ψ_θ , we assume that we have training samples \mathbf{x} from X with noisy versions \mathbf{x}_σ from $X_\sigma = X + \sigma\eta$ with $\eta \sim \mathcal{N}(0, I)$. After choosing a loss function ℓ , we can learn Ψ_θ by solving

$$\hat{\theta} = \arg \min_{\theta} \mathbb{E}_{\mathbf{x}, \mathbf{x}_\sigma} [\ell(\mathbf{x}, \Psi_\theta(\mathbf{x}_\sigma))]. \quad (49)$$

Common choices for ℓ are the square error $\ell(\mathbf{x}, \mathbf{y}) = \|\mathbf{x} - \mathbf{y}\|_2^2$, or the absolute error $\ell(\mathbf{x}, \mathbf{y}) = \|\mathbf{x} - \mathbf{y}\|_1$.

Unfortunately, neither of these choices leads to the desired **MAP** denoiser in (49): as mentioned in Section 1, choosing the square error leads to the **MMSE** estimator, while the absolute error leads to a generalization of medians [66]. To enforce that the minimizer of (49) leads to $\text{prox}_{-\sigma^2 \log p_X}$, the authors in [50] propose the **proximal matching (PM)** loss

$$\ell_\gamma(\mathbf{x}, \mathbf{y}) = 1 - \frac{1}{(\pi\gamma^2)^{d/2}} \exp\left(-\frac{\|\mathbf{x} - \mathbf{y}\|_2^2}{\gamma^2}\right), \gamma > 0. \quad (50)$$

They show that the denoiser $f^* = \arg \min_f \text{measurable} \lim_{\gamma \searrow 0} \mathbb{E}_{\mathbf{x}, \mathbf{y}} [\ell_\gamma(\mathbf{x}, f(\mathbf{y}))]$ satisfies $f^* = \text{prox}_{-\sigma^2 \log p_X}$ almost everywhere [50, Thm. 3.2]. In practice, we minimize (49) for $\ell = \ell_\gamma$ with decreasing values of γ to approximate the limit $\gamma \rightarrow 0$, see also [50, App. G]. If the architecture Ψ_θ is universal, then one obtains the proximal operator of $R = -\sigma^2 \log p_X$. Importantly, this denoiser Ψ_θ —as it reflects the prior p_X —can be readily deployed within the variational problem (2) for other inverse problems using the ADMM algorithm [33]. If Ψ_θ is parametrized as **LPN**, then convergence of the resulting **PnP-ADMM** iterations to fixed points can be guaranteed, see [50] for details.

4 Set-Up for Comparative Study

Now, we describe the setup for our experimental comparison. We built upon the **DeepInverse** library [141], and our code is available on [GitHub](#).

4.1 Minimization of the Variational Problem

For most architectures, we minimize (2) via the [nonmonotonic Accelerated Proximal Gradient algorithm \(nmAPG\)](#) [90, Suppl.]. This method builds upon the ideas of FISTA [20]. By ensuring sufficient decrease on an auxiliary objective, it guarantees convergence to a stationary point for non-convex problems while maintaining the optimal convergence rate of $\mathcal{O}(1/k^2)$ on convex problems. A backtracking linesearch with Barzilai–Borwein initialization ensures convergence even without knowledge of the Lipschitz constant of the gradient. The stopping criterion is based on the relative step size. See [GitHub](#) for details. For some architectures, the [nmAPG](#) is infeasible and we use a different optimization method for minimizing (2):

- For the patch-based regularizers R in (13), the evaluation cost scales linearly with the number of patches s , making it prohibitive for high-resolution images. To address this, we instead evaluate R only on a random subset of patches per iteration [5]. For both [EPLL](#) and [PatchNR](#), we solve the variational problem (2) using [Adam](#) with a cosine-annealed step size schedule.
- While [LPNs](#) provably define a regularizer R , the latter is only given implicitly via its proximal mapping. Therefore, we evaluate [LPNs](#) with a plug-and-play algorithm based on the alternating direction method of multipliers [33], where the implementation from [DeepInverse](#) is used.

4.2 Forward and Noise Models

We consider two (inverse) problems: denoising and [CT](#) reconstruction. The latter has become one of the most accessible imaging modalities in non-destructive testing, security, and medicine. For denoising, it holds that $\mathbf{H} = \mathbf{I}$. Additionally, the images $\mathbf{x} \in [0, 1]^d$ are corrupted by additive Gaussian noise \mathbf{n} with standard deviation $\sigma = 0.1$. Regarding our [CT](#) reconstruction experiment, recall that a scanner acquires multiple measurements while rotating around an object. We model a sparse-view setting, where \mathbf{H} is given by the discretized X-ray transform with 60 equispaced angles and a parallel beam geometry. We use the [DeepInverse](#) implementation. To keep the setup simple, we consider Gaussian noise with $\sigma = 0.7$ instead of more realistic Poisson noise. For our ground truth images $\mathbf{x} \in [0, 1]^d$, the measurement range is between 0 and 400. In both settings, we use the data-fidelity $D(\mathbf{Hx}, \mathbf{y}) = \frac{1}{2}\|\mathbf{Hx} - \mathbf{y}\|^2$. For [CT](#) reconstruction, taking the pseudo-inverse \mathbf{H}^\dagger is also known as [filtered backprojection \(FBP\)](#).

4.3 Datasets

For denoising, we use the BSDS500 dataset [10, 95], which contains 500 color images of size 481×321 of mixed landscape and portrait orientation. To simplify the setup, we convert them to grayscale. The dataset is split into 400 images for training and validation, and the 68 images of the BSD68 set for testing. Following the literature, the remaining 32 test images are discarded.

For the [CT](#) reconstruction experiments, we consider the LoDoPaB-CT dataset [89]. Its ground truth images of size 362×362 are based on reconstructions in the LIDC/IDRI database [13]. While the original dataset is very large, we use the 3522 images from the validation set for training, and the 128 images from the first test batch for testing.

4.4 Experiments and Evaluation Metric

Within the setup of Sections 4.2 and 4.3, we conduct three experiments.

1. **Denoising for Natural Images:** We perform denoising of the BSDS500 dataset. In the reconstruction step, we choose the same regularization parameter α in (2) for training and testing since the setups coincide.

2. **Generalization to CT Reconstruction:** We evaluate the generalization capability of the trained R_θ from the first experiment. To this end, we insert $\tilde{R}_{\alpha,s}(\mathbf{x}) = \frac{\alpha}{s^2} R_\theta(s\mathbf{x})$ into (2) and fine-tune the regularization and scaling parameters α and s on the first five images from the training split of the LoDoPaB-CT dataset. Instead of a grid search, we use our bilevel training method with hypergradients computed by [IFT](#).
3. **Learned CT Reconstruction:** Both domain-specific data (LoDoPaB-CT dataset) and the forward operator \mathbf{H} are available for learning R_θ . The results are expected to improve upon the ones from the second experiment.

We evaluate all results using the [peak signal-to-noise ratio \(PSNR\)](#) defined for the ground truth image \mathbf{x} and reconstruction $\hat{\mathbf{x}}$ as

$$\text{PSNR}(\hat{\mathbf{x}}, \mathbf{x}) = 10 \cdot \log_{10} \left(\frac{d^2 r^2}{\|\hat{\mathbf{x}} - \mathbf{x}\|^2} \right), \quad (51)$$

where d is the number of pixels and r is the range of the pixel values. For the denoising problem, we choose $r = 1$. For the [CT](#) reconstruction experiments, we choose $r = \max_{i,j}(\mathbf{x}_{ij})$, namely the maximal pixel value in the ground truth image.

4.5 Architectures

Below, we specify the configurations of each regularizer in the comparison.

CRR and WCRR The multiconvolution consists of 3 blocks, where the kernels have size $k = 5$ with 4, 8 and 64 output channels, respectively. This corresponds to $c = 64$ kernels with an effective size of 13. For the [CRR](#), we use the potential ψ^β from (8), and for the [WCRR](#), we use the modified potential $\tilde{\psi}^\beta = \psi^\beta - \psi^1$, where in both cases parameter β is learnable.

ICNN We use two convolution layers with no skip connection as shown in (11). The kernels have size $k = 5$ with 32 output channels. The learnable smoothing parameter β for the [ReLU](#) is initialized as 100.

IDCNN The [IDCNN](#) is constructed as the difference of two [ICNNs](#). The general architecture of the [ICNNs](#) is the same as described above, where the activation is changed to [ELU](#) [36] with $\alpha = 1$ for the [AR](#) result in Table 5. In this particular case, changing the activation significantly improved the reconstruction quality.

EPLL We employ [GMMs](#) with 100, 200, 300, 400 components and patches of size 6×6 and 8×8 . The exact number of components and patch size are selected based on the validation set.

PatchNR For the [NF](#) we employ 10 affine coupling layers. Each layer uses a single three-layer MLP with [SiLU](#) activations [69] and a hidden dimension of 512. The output of the MLP is split into two parts to obtain the scale s and translation t in (16). The final layer of the MLP is zero-initialized to ensure that the invertible neural network initially equals the identity.

CNN We use 6 convolutional layers with 3×3 kernels. The choice of the architecture implicitly defines the patch size as 15×15 , following [122]. As the activation function, we deploy the differentiable [SiLU](#).

TDV We use the [TDV](#)³, which consists of $b = 3$ macro-blocks each operating on $a = 3$ scales. We use $c = 32$ kernels for the convolution layers. All kernels of the first layer \mathbf{W} have zero mean.

LSR We choose U as a DRUNet [157] with softmax activation and four scales, where each scale consists of two residual blocks with 32, 64, 128 and 256 channels. For the [NETT](#) training, we choose U as a [CNN](#) consisting of 7 layers with 3×3 kernels, 64 hidden channels and an additional residual connection at the end. The activation function is given by [CELU](#) [19] with $\alpha = 10$.

LPN We realize the network Φ_θ from (21) as an **ICNN** consisting of 7 convolution layers with 256 hidden channels. Every second convolutional layer has stride 2 instead of 1. After each downsampling, a skip connection injects the (downsampled) input image. For the activation function, we choose softplus with $\beta = 100$. The **ICNN** operates on patches of size 64×64 and is applied to larger images using a sliding window with stride 32.

4.6 Training Methods

Below, we specify the hyperparameters of the deployed training methods. We always save the checkpoint with the best validation score.

SM We train using the **SM** loss (47) with $\sigma = 0.03$. For the deployed Adabelief optimizer [161], the learning rate and the number of epochs depend on R_θ . As post-processing, we fit α and s as detailed in Section 4.4. The resulting θ_{SM} is also used as initialization for the **BL-IFT** and **BL-JFB** approaches. To initialize the methods in Table 5, we instead use $\sigma = 0.015$ and add weight decay in order to achieve more regularity.

BL-IFT We initialize with the θ_{SM} generated by the **SM** routine. Then, we train R_θ with the bilevel loss (25) and $G_x = \|\cdot - x\|_2^2$ using the Adabelief optimizer together with the **IFT** to compute the hypergradients. The accuracies for solving the lower-level problem and the linear system for the hypergradients are both set to 10^{-4} . Further, the learning rate and the number of epochs depends on R_θ . To improve stability, we apply Hessian norm regularization every 5 epochs.

MAID We adopt an Adagrad update [44, 150] with preconditioner $1/\sum_{t=0}^k |z_t|$, where z_t is the approximate hypergradient at a successful iteration t of Algorithm 1. The training dataset consists of a fixed number of patches, depending on R_θ . For the hyperparameters in Algorithm 1, we use $\underline{\rho} = 0.5$, $\bar{\rho} = 1.25$, $\underline{\nu} = 0.5$, $\bar{\nu} = 1.05$, a maximum of backtracking iterations $b = 5$, and initial accuracies $\epsilon_0 = \delta_0 = 10^{-1}$. In contrast to [132], we only check for a decrease in the function value in Step 6 of Algorithm 1.

BL-JFB We adopt the **JFB** approach (33) with $k_b = 1$ to compute the hypergradients. Everything else remains the same as for **BL-IFT**.

NETT We use the **Adam** optimizer with a learning rate of 10^{-4} to minimize (37). After the training, we fit α as detailed in Section 4.4.

AR/LAR We minimize the **AR** objective (38) using **Adam**. To reduce the computational burden, we actually train on patches, which amounts to **LAR**. The patch and batch size, learning rate, decay rate, and epochs depend on R_θ . After the training, we finetune α and s as detailed in Section 4.4.

PatchML To minimize the **PatchML** objective (44), we use the **Expectation-Maximization (EM)** algorithm as implemented in **DeepInverse** for **EPLL** and gradient-based optimization with **Adam** for **PatchNR**. After training, we fit the regularization parameter α using a grid search.

PM We pretrain the model with the ℓ_1 loss for 160k iterations with a learning rate of 10^{-3} . Then, we continue training with the **PM** loss (50) for another 160k iterations using a learning rate of 10^{-4} . The parameter γ is initialized as $1.28\sqrt{n}$ and reduced by half every 40k iterations, where n is the data dimension. To ensure that the **ICNN** (which parameterizes the **LPN**) remains convex, we clip its weights after each training step to ensure their non-negativity. The batch size is 64 for BSDS500 and 128 for the LoDoPaB-CT dataset.

4.7 Baseline Methods

In addition to the learned regularizers, we report the **PSNR** values for some common baselines. We use the regularization parameter or the checkpoint with the lowest **mean squared error (MSE)** on the validation set.

TV We consider the variational problem (2) with R chosen as the anisotropic **TV** [131]. To minimize (2), we employ the **primal-dual hybrid gradient (PDHG)** algorithm [32, 119]. For denoising, the reconstruction **PSNR** is 27.30 dB, and for the **CT** setup, we achieve a **PSNR** of 30.99 dB.

DRUNet [157] We use the implementation and weights from **DeepInverse**, which achieves a reconstruction **PSNR** of 29.41 dB. Both the training set and the model size (32.6M parameters) are significantly larger than any of the regularizers that we test in this work, see also Table 3.

FBP+UNet Our UNet-based postprocessing [79] for **CT** is implemented using **DeepInverse**. In this approach, the output of the **FBP** is inserted into a UNet. The latter is trained to remove artifacts by minimizing the **MSE** against the ground truth images. The UNet uses 5 scales and has approximately 34.5M parameters. We train with **Adam** for 100 epochs with a learning rate of 10^{-3} . This leads to a reconstruction **PSNR** of 33.03 dB.

Learned primal-dual (LPD) This **CT** reconstruction method [1] unrolls the **PDHG** for a fixed number of steps and replaces the proximal operators with **CNNs**. We use 6 steps and implement the networks for the dual variables as small **CNNs**, whereas the networks in the primal space are UNets. This results in roughly 1M parameters. As in [67], we replace the adjoint \mathbf{H}^T in **LPD** with the **FBP**. The model is trained for 100 epochs using an initial learning rate of 10^{-4} with a cosine decay to 10^{-6} . This leads to a reconstruction **PSNR** of 33.71 dB.

5 Numerical Results

5.1 Experiment 1: Denoising

The regularizers are trained and evaluated for denoising of natural images. Quantitative results are reported in Table 3. Some training methods work only with specific regularizers, so not all combinations are compatible. These fields are grayed out. Additionally, we use a hyphen for fields that could be filled out, but where the run was computationally intractable or unstable.

The convex models (**CRR** and **ICNN**) behave similarly, and their performance is largely unaffected by the chosen training scheme. In particular, the unsupervised **SM** and the semi-supervised **AR** yield similar results as the supervised bilevel training. To some extent, this is also true for **WCRR**. The nonconvex **WCRR**, **IDCNN**, **CNN** and **LPN** lead to similar **PSNR** values. The patch-based regularizers (**EPLL** and **PatchNR**) are not competitive. The best results are achieved by **TDV** and **LSR** if trained via bilevel learning. Here, the specific routine (**BL-IFT**, **BL-JFB**, **MAID**) has negligible impact. With the other training routines, the performance of the nonconvex architectures degrades heavily.

Qualitative results are shown in Figure 3. The trend is similar to Table 3, in that convex models lead to the worst image quality and architectures with the highest number of parameters (**TDV** and **LSR**) lead to the best image quality overall. Interestingly, the nonconvex models reconstruct the geometry of the large window wrongly. In particular, **TDV** and **LSR** produce visually appealing windows that differ significantly from the ground truth (see Figure 3).

Figure 4 illustrates the influence of the training scheme, exemplified here for the **TDV** regularizer. The bilevel training yields good approximations of the ground truth, comparable to those of DRUNet. **AR** leads to a smoother image with fewer details and **SM** yields a cartoonish looking image with sharp edges.

5.2 Experiment 2: Generalization to CT

We investigate how the models from Experiment 1 generalize to **CT** reconstruction of medical images. Quantitative results can be found in Table 4. As there was no significant difference between the bilevel methods in Experiment 1, we report results only for **BL-JFB**. Overall, there are similar trends as for

Table 3. Almost all methods perform better than **TV** even though they have not been trained on the underlying data. This means that they generalize fairly well.

Reconstructions can be found in Figure 5. Here, none of the variational methods yields sharp images comparable to the ground truth. This is in contrast to the supervised baselines (**FBP+UNet** and **LPD**), which give sharper images with higher **PSNR**. The patch-based regularizers (**EPLL** and **PatchNR**) yield performance comparable to that of **CRR** and **ICNN**. This contrasts the results in Table 3 even though the same weights are used for both experiments.

5.3 Experiment 3: CT-specific Training

The regularizers are trained and evaluated on **CT** reconstruction of medical images. Due to computational reasons, we only consider the **BL-JFB** mode of bilevel learning. Quantitative results are reported in Table 5. Overall, similar observations can be made as before. For **BL-JFB**, the convex models (**CRR** and **ICNN**) already perform significantly better than **TV**. The performance improves slightly for the fairly simple nonconvex and patch-based models **WCRR**, **IDCNN**, **EPLL** and **PatchNR**. The high-parametric models **TDV** and **LSR** achieve the highest **PSNR**. For **AR** training, the difference is much smaller, with convex models and **IDCNN** performing slightly worse than other architectures. As before, the training scheme is important for the more complex architectures.

The quantitative results are visually confirmed in Figure 6. **TDV** and **LSR** give well-defined structures with crisp details that are fairly consistent with the ground truth. **LSR** achieves the best **PSNR** for this image, in line with the results on the whole dataset. Note that **TDV** and **LSR** are on par with the **LPD** baseline. In summary, the task-specific training greatly enhances the visual reconstruction quality compared to Figure 5. Figure 7 shows visual results for different training methods applied to **LSR**, highlighting the outcomes of Experiments 2 and 3 using **BL-JFB** and **NETT**.

5.4 Training Times for Experiment 1

So far, we only highlighted the image quality, both quantitatively and qualitatively, after the training has been completed. Now, we analyze the computational load incurred during training. To ensure comparability, all experiments are conducted on a single NVIDIA GeForce RTX 4090 GPU with 24 GB memory. In Table 6, we report the training times for Experiment 1 in hours for all methods. In all cases, the models were trained until the loss stabilized. There are some trends to be observed. First, simpler models like **CRR**, **WCRR**, and to a certain extent **ICNN**, required the shortest training time, mostly under an hour. In contrast, more complex architectures like **IDCNN**, **CNN**, **TDV** and **LSR** required significantly longer training time, ranging from several hours to up to 2 days. Furthermore, **SM** tends to be cheaper than **AR**, which in turn tends to be cheaper than bilevel learning. In all experiments, **BL-JFB** was consistently faster than **BL-IFT** while leading to similar results.

For bilevel training, we implemented three algorithms: **BL-IFT**, **BL-JFB** and **MAID**. These differ in how they compute hypergradients and how they treat solver tolerances and step sizes. Figure 8 compares them for training a **CRR**. For this, we drop the **SM** pretraining since this already leads to nearly optimal parameters (Table 3). In the top row, we see the training and validation **PSNR**. From the training graph, it is clearly visible that **BL-IFT** and **BL-JFB** are stochastic methods, whereas the implemented **MAID** version is nonstochastic. We tuned the hyperparameters to maximize the validation **PSNR**. The respective test performances are compared in the bottom row. All three approaches converge to a similar **PSNR**, with **BL-IFT** being best. Interestingly, **MAID** reaches a near-optimal **PSNR** already after around 200 seconds, which is almost twice as fast as the other methods. Potential explanations are the lower level accuracy in early iterations, and the much larger step sizes (on average 100 times larger).

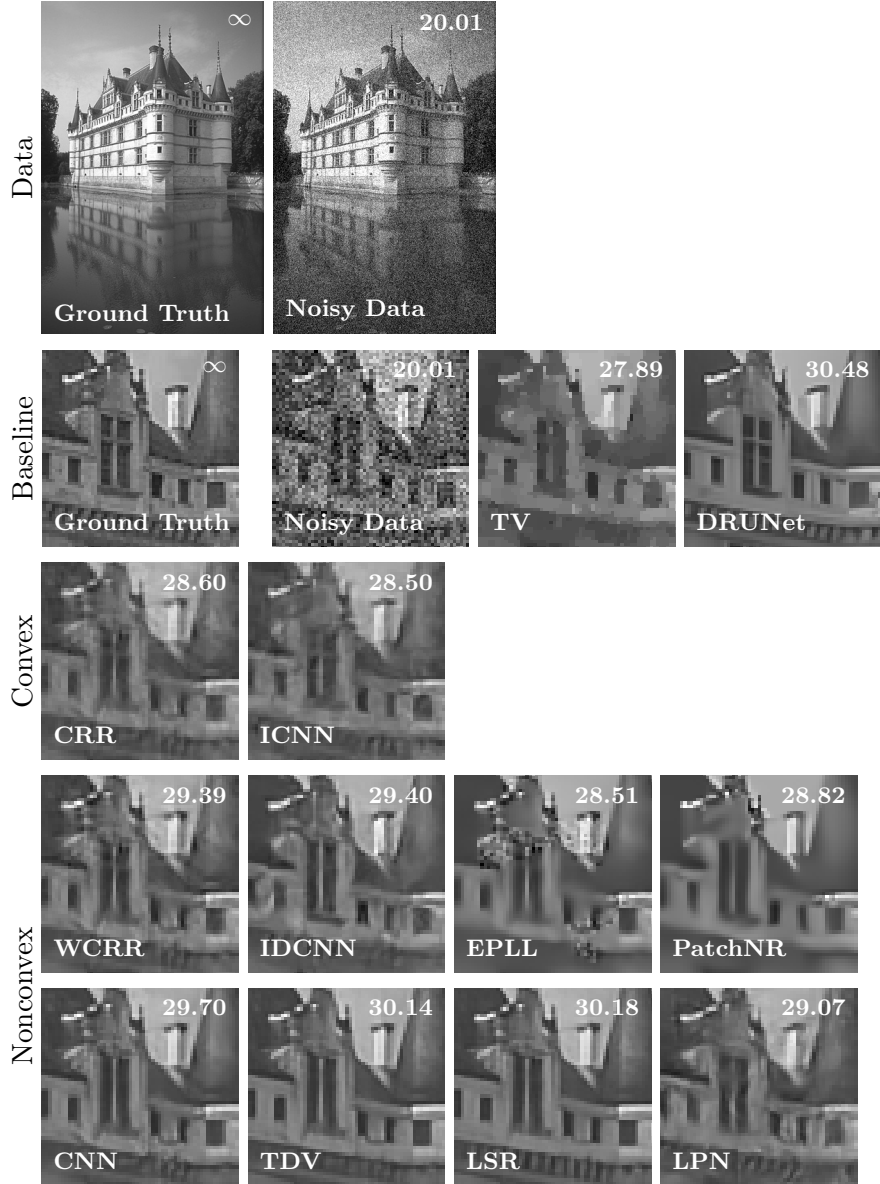


Figure 3: Denoising result for Experiment 1 on test image 'castle' from BSD68.

5.5 Evaluation Times for Experiment 1

Finally, we compare the reconstruction times when solving the variational problem (2). Again, we use a single NVIDIA GeForce RTX 4090 GPU with 24 GB memory. Table 7 reports the average runtime of `nmAPG` in seconds until the convergence criterion is reached. For most combinations of architecture and training scheme, the runtime is below 1 second. The `CRR`, `WCRR`, `ICNN`, `IDCNN` are faster than the others with maximal speed of around 0.1 seconds reached by `ICNN` when trained via `SM` or `AR`. More complex architectures tend to need longer with runtimes of 1-2 seconds. The ratio between the slowest and the fastest method is around 50. Due to the many overlapping patches, both `EPLL` and `PatchNR` have a slow algorithmic performance. Note that their evaluation could be accelerated by stochastic optimization methods or by using the half-quadratic splitting scheme, which was originally used for `EPLL` [113, 162].

Table 3: Experiment 1: **PSNR** (in dB) for denoising results on BSD68 with $\sigma = 0.1$. All models are trained for denoising on BSDS500. **TV**-denoising leads to a **PSNR** of 27.3 and a DRUNet reconstruction to 29.41. The classic **EPLL** with half-quadratic splitting gave a **PSNR** of 28.46.

Architecture: CRR ICNN WCRR IDCNN CNN TDV LSR EPLL PatchNR LPN									
Training Scheme	BL-IFT	28.01	27.90	28.60	28.58	-	29.24	29.25	
	BL-JFB	28.00	27.89	28.59	28.57	28.89	29.24	29.27	
	MAID	28.01	27.82	28.54	-	-	-	-	
	AR/LAR	27.96	27.77	28.48	28.20	28.34	28.62	-	
	NETT							27.09	
	SM	27.94	27.73	28.48	27.93	27.59	27.96	27.61	
	PatchML						27.46	27.74	
	PM								28.33

Table 4: Experiment 2: **PSNR** (in dB) for **CT** reconstruction on the LoDoPaB-CT data set. All models are trained on BSDS500 **without** using the operator **H**. The **TV** reconstruction achieved a **PSNR** of 30.99 and **FBP** of 19.98. For BL we report the best-performing instance from Experiment 1.

Architecture: CRR ICNN WCRR IDCNN CNN TDV LSR EPLL PatchNR LPN									
Training Scheme	BL (best)	32.17	31.99	32.65	32.45	32.69	33.23	33.11	
	AR/LAR	32.14	31.94	32.61	31.98	32.04	32.43	-	
	NETT						30.64		
	SM	32.12	31.85	32.32	31.76	30.03	32.32	30.26	
	PatchML						31.94	32.17	
	PM								31.29

Table 5: Experiment 3: **PSNR** (in dB) for **CT** reconstruction on LoDoPaB-CT data set. All models are trained on LoDoPaB-CT images using the operator **H**. The **TV** reconstruction achieved a **PSNR** of 30.99 and **FBP** of 19.98. The learned **FBP+UNet** achieved a **PSNR** of 33.03 and **LPD** of 33.71.

Architecture: CRR ICNN WCRR IDCNN CNN TDV LSR EPLL PatchNR LPN									
Training Scheme	BL-JFB	32.30	32.16	32.85	32.56	-	33.67	33.72	
	AR/LAR	32.23	31.98	32.48	31.93	32.29	32.33	-	
	NETT						32.01		
	PatchML						32.55	32.63	
	PM								32.08

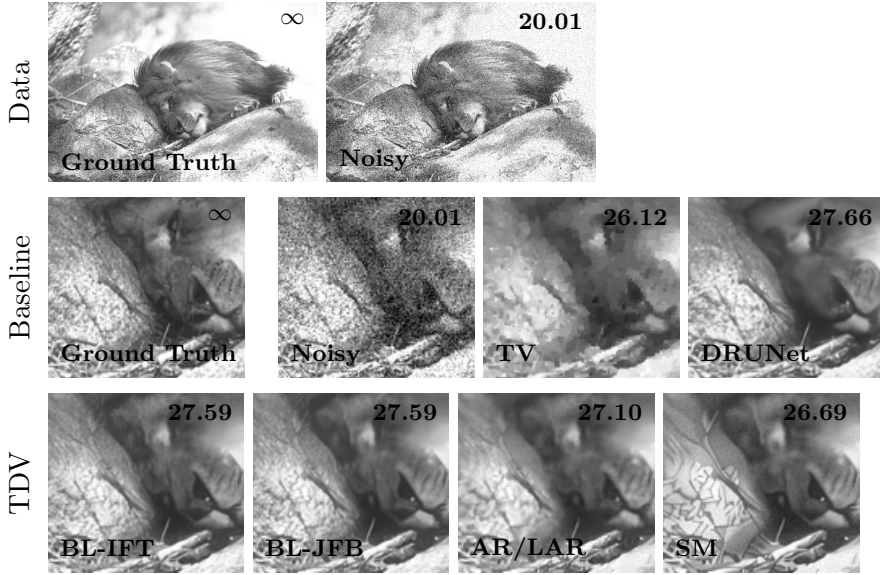


Figure 4: Experiment 1: Comparison of training schemes on 'lion' image from BSD68.

Table 6: Experiment 1: Training time in hours.

Architecture: CRR ICNN WCRR IDCNN CNN TDV LSR EPLL PatchNR LPN								
Training Scheme	BL-IFT	0.8	3.0	1.0	26.9	-	11.6	41.2
	BL-JFB	0.5	0.8	0.7	2.7	7.3	7.1	13.3
	MAID	0.2	0.3	0.1	-	-	-	-
	AR/LAR	0.2	0.5	0.2	4.5	2.7	3.1	-
	NETT						11.0	
	SM	0.1	0.3	0.1	0.9	0.3	3.6	9.2
	PatchML						3.7	0.5
	PM							15.2

Table 7: Experiment 1: Reconstruction times per image in seconds.

Architecture: CRR ICNN WCRR IDCNN CNN TDV LSR EPLL PatchNR LPN								
Training Scheme	BL-IFT	0.80	0.19	0.46	0.19	-	1.07	1.57
	BL-JFB	0.32	0.15	0.50	0.45	1.93	1.21	2.28
	MAID	0.67	0.12	0.32	-	-	-	-
	AR/LAR	0.34	0.11	0.36	0.24	1.11	1.09	-
	NETT						1.09	
	SM	0.26	0.09	0.28	0.31	1.17	1.71	4.34
	PatchML						77.23	5.37
	PM							0.27

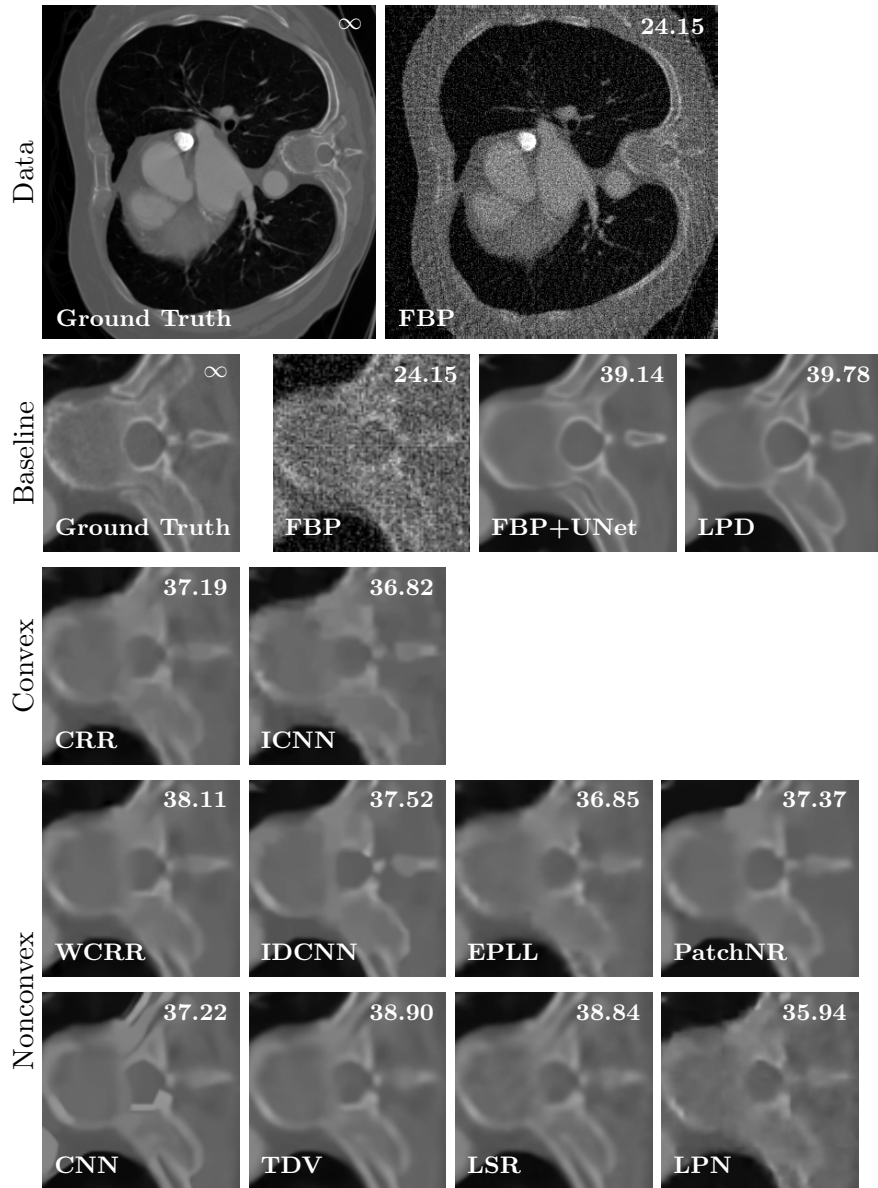


Figure 5: CT reconstructions for Experiment 2 on a test image from LoDoPaB-CT.

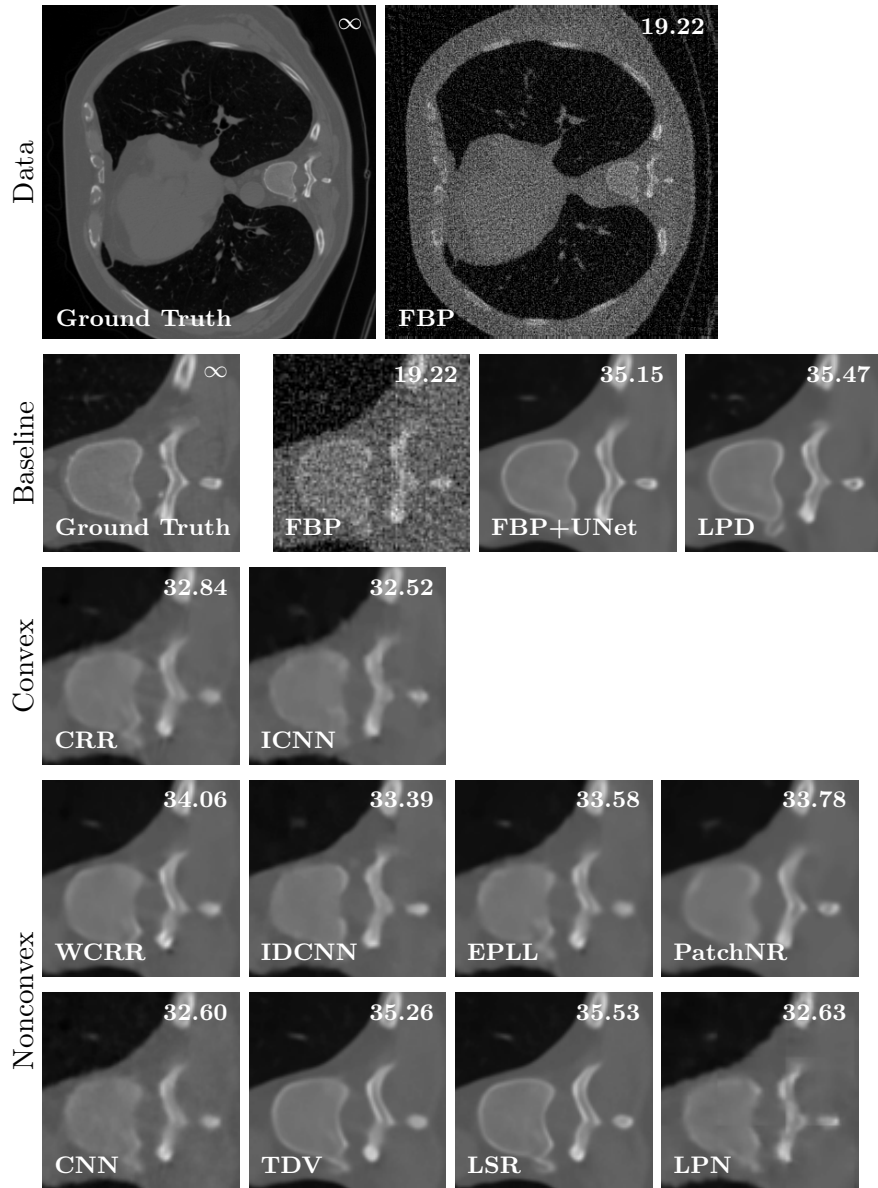


Figure 6: CT reconstructions for Experiment 3 on test image from LoDoPaB-CT.

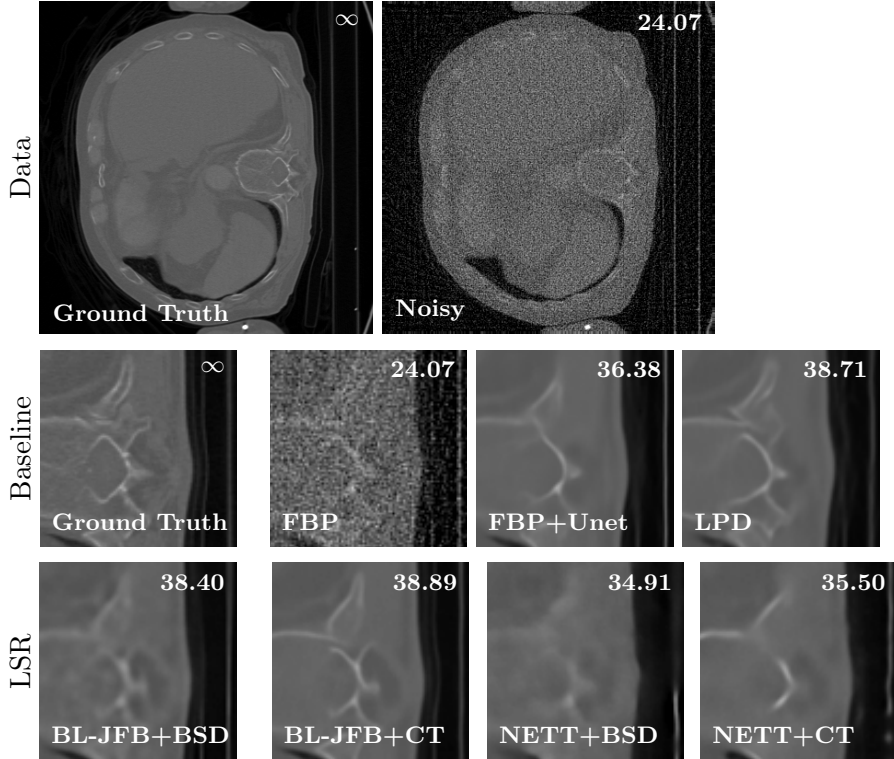


Figure 7: Comparison of training schemes to learn **LSR** for **CT** reconstruction. The test image is from LoDoPaB-CT, and the “+BSD” and “+CT” refer to Experiments 2 and 3, respectively.

6 Discussion

In Experiment 3, the larger architectures, such as **TDV** and **LSR** with bilevel training, yield the sharpest reconstructions and highest **PSNR** values. Their performance is comparable with end-to-end reconstruction networks like **FBP+UNet** or **LPD**, which, however, cannot be interpreted as variational reconstruction. Moreover, the latter methods may introduce additional structures (hallucinations) in the reconstructions to resemble the training data more closely. To a much lesser extent, this also occurs for **TDV** and **LSR**. We did not detect such artifacts for the other regularizers used in our experimental comparison. Thus, we can consider learned regularization as a robust and reliable method.

As discussed in detail below, another big advantage of learning regularizers is that they can be trained without using the operator **H** and domain-specific data. Hence, as a universal pretrained model, learned regularization can be a readily accessible tool in many applications, even when reliable ground truth data is not available. Nevertheless, if computationally feasible, finetuning with task-specific data and the operator **H** will improve the **PSNR** and visual reconstruction quality.

Regularizer Architectures The discussed regularizers offer a trade-off in terms of theoretical guarantees, computational cost and expressivity. Taking bilevel learning as an example, there is a large gap between convex architectures (like **CRR** and **ICNN**) and large nonconvex architectures (like **TDV** and **LSR**) in terms of visual reconstruction quality and **PSNR**. Although slight relaxations of convexity (as in **WCRR** and **IDCNN**) lead to improved performance, they cannot close the performance gap to large architectures. Interestingly, the additional flexibility of **ICNNs** over the **CRR** seems to not improve the results in terms of **PSNR**. Our implementation of **CRR** requires fewer parameters, is easier to train and leads to better results. An open question is whether other parameterizations of

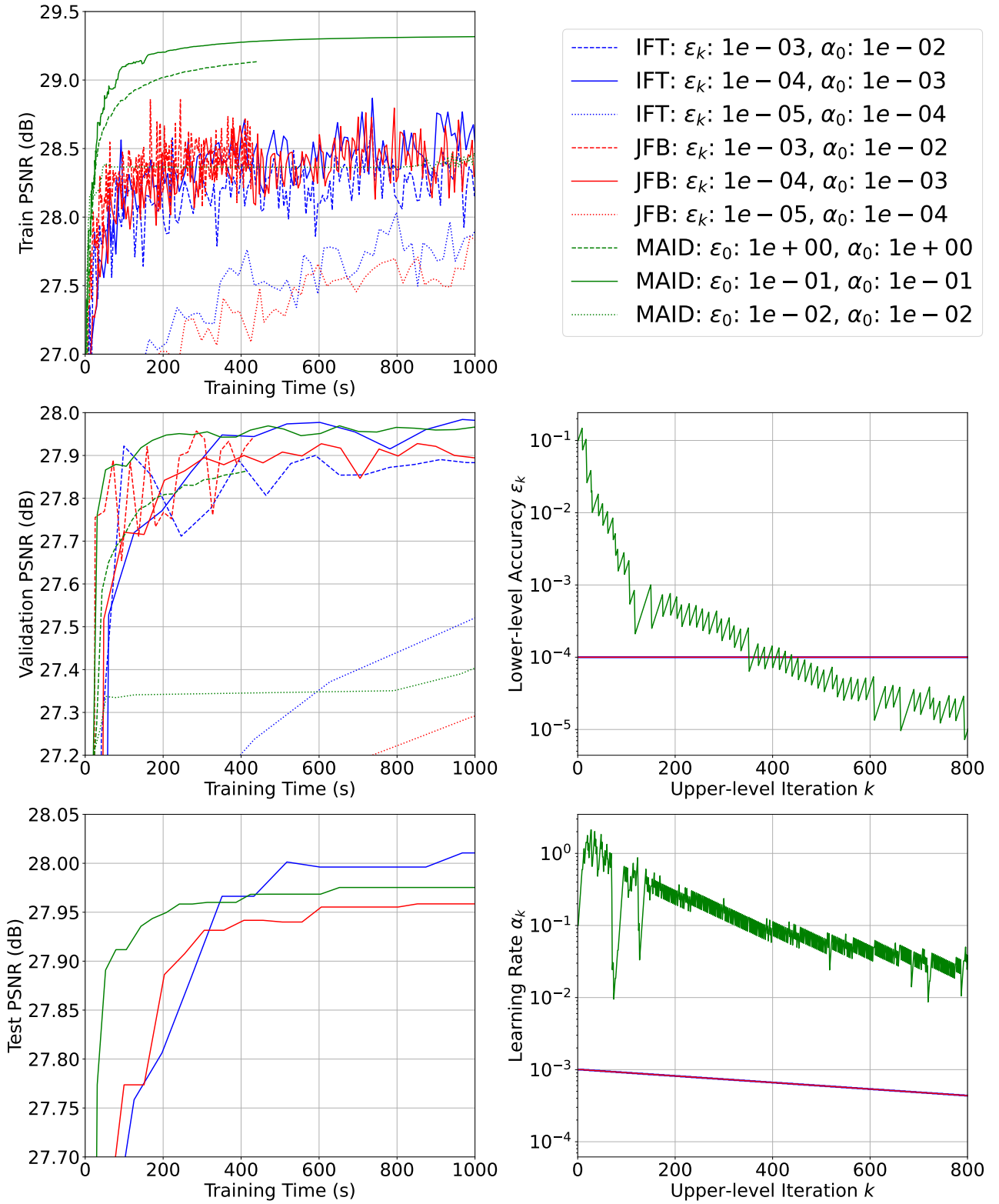


Figure 8: Training time comparison between MAID, BL-IFT and BL-JFB for CRR. All algorithms converge to a very similar test PSNR but vary in speed.

the **ICNN** can overcome this behavior. Moreover, nonconvex extensions do not necessarily behave like their convex counterparts. As an example, **WCRR** aligns more closely with **CRR** than **IDCNN** with **ICNN**, especially regarding training time.

For denoising, we also compared with the learned DRUNet denoiser, whose performance is closely matched by **TDV** and **LSR** despite having an order of magnitude fewer parameters. For the practically more relevant **CT** reconstruction, both **TDV** and **LSR** are competitive with end-to-end reconstruction networks such as **FBP+UNet** and **LPD**.

Training Methods Among the investigated training methods, **BL-IFT/BL-JFB** consistently achieved the highest **PSNR** values. However, it also requires the longest training times. In this regard, **AR** and **SM** provide more efficient alternatives, both in terms of time and memory consumption. Notably, for simple (convex) regularizers, these semi-supervised/unsupervised methods achieve reconstruction results that are comparable to those of **BL-JFB**. This makes **AR** a serious alternative for scaling these models to higher dimensions and larger datasets. However, nearly optimal performance of **AR** is already achieved by the **WCRR** and more complex regularizers did not improve. Thus, we regard **BL-JFB** as the gold standard when sufficient computational resources and supervised training data are available. In particular, the results in Table 4 indicate that the learned models possess strong generalization capabilities. As a consequence, one may train only for denoising and subsequently adjust the parameters α and s (see Section 4.4), which is often substantially more efficient than training with the operator **H**.

To further improve the computational efficiency, patch-based training of reconstruction networks is nowadays the standard for tasks where **H** can be evaluated on patches. In this case, the goal is not to approximate a patch distribution but to speed-up the training process. Notably, the patches used in this context are typically much larger than those for methods discussed in Section 2.5. For our experiments, we used patches of size between 25×25 and 80×80 , depending on the field-of-view of the regularizer. While we found patches to be beneficial for all presented methods, they were particularly important for **AR** training in the setting of **CT** reconstruction. In summary, we advise to always train on patches if possible, both from a stability and efficiency perspective.

We conclude with a remark on **NETT**. There, both the training/validation losses decrease consistently throughout training, but the reconstruction quality often deteriorates beyond some point. This behavior is even more severe than for **AR**, and a reason for this could be the lack of a regularizing term in the loss (37) compared to (38). The latter helps to prevent overfitting.

Different Variants of Bilevel Learning Across our experiments, all bilevel methods have led to comparable reconstruction performance. In practice, the **IFT** mode is only feasible if the Hessian-vector products can be computed efficiently, or in strongly convex settings where linear solvers converge in a few steps. Otherwise, it is computationally infeasible. Since the computationally much more efficient **JFB** mode consistently matched or even outperformed the **IFT** mode, we recommend it as the default choice.

For the **IFT** and **JFB** modes, we found it beneficial to employ **SM** pretraining together with Hessian regularization, in line with prior observations [163]. The latter also reduces the number of steps required by the **nmAPG** during evaluation, a property that is not promoted by the plain bilevel objective (25). After incorporating these elements, the results were consistent across multiple training runs. This contrasts **AR** and **NETT**, both of which exhibit high variance between runs. A source for this behavior could be the relatively small datasets, where overfitting a classifier is likely.

The **JFB** and **IFT** mode both assume convergence of the involved iterative solvers, which requires hand-tuning the corresponding accuracies and step sizes. **MAID** provides a method to choose them adaptively, which can speed up the optimization and guarantees convergence. However, currently it does not support stochastic optimization in the upper-level solver and the theoretical analysis requires

the lower-level problem to be convex. Moreover, it relies on the computationally more expensive **IFT** mode. Therefore, it is only applicable for small (weakly) convex architectures for which the numerical results from the previous sections show similar performance as for **JFB** and **IFT**. Addressing these shortcomings remains subject of future work.

Solving the Variational Problem To keep the comparison manageable, we only used **nmAPG** to solve the variational problem (2), which worked well for all the tested regularizers. From an application perspective, a fast minimization of (2) is key to scaling the approach and it plays an important role during the bilevel training approaches. In this chapter, however, we placed the focus on reconstruction quality, and faster convergence was not encouraged during training. A comparison with other algorithms would be interesting but is beyond the scope of this chapter.

Once the regularizer R is fixed, one can investigate properties of the variational problem (2), and in particular, the properties of the resulting variational solution itself. For the **NETT** [91] and **AR** [93, 138] frameworks, it has been shown that plugging the learned regularizer into (2) yields a well-posed regularization method: solutions exist, the data-to-reconstruction map is continuous, and suitable parameter choice rules lead to convergence for vanishing noise. Stronger continuity results in the measurement domain can be obtained for convex regularizers [55, Prop. 3.2]. A related result involving spatially varying Λ (see Section 2.1) has been derived in [84, Prop. 6] for conditional **TV** regularization. Several generalizations and an extension to uncertainty in the data \mathbf{y} itself can be found in [105]. For a recent overview, we refer to [102].

Limitations This chapter provides a comparison of regularizer architectures and training schemes. To this end, we unified the training and evaluation setting as much as possible. Due to time constraints, certain aspects are not investigated systematically. In particular, we did not examine how the reconstruction performance depends on the dataset size. Furthermore, in many practical applications the operator \mathbf{H} is subject to modeling errors and the Gaussian noise assumption may not hold; robustness of the learned regularizers to such settings is not addressed. For bilevel learning, alternative upper-level loss functions have been proposed, including **MSE**, L_1 , **PM**, **LPIPS** [159], and **TV** [40]. These might affect the reconstruction performance noticeably. Likewise, methods for quantifying uncertainty in reconstructions, though highly relevant, were not considered.

We also note that not all entries are filled in Tables 3, 4, and 5. Some regularizers (e.g., **EPLL**, **PatchNR**, **LPN**) can only be trained in specific ways. For **LSR**, training occasionally exhibited instabilities that prevented further comparisons. The training algorithm **MAID** requires convexity of the variational problem (2), which is only fulfilled for convex or weakly-convex regularizers. Generalizations remain outside the scope of this chapter.

Extensions In this chapter we focused on the comparison of existing learned regularizers and training methods. Interesting extensions of the current methods are the inclusion of the noise level as input of the regularizer, or properties of the operator \mathbf{H} such as source conditions [103]. It would also be interesting to investigate if there is a benefit of training a regularizer on several inverse problems at once, i.e., can we learn a foundational model for general inverse problems. Further, a systematic analysis and evaluation of learned regularizers with respect to their theoretical properties would be highly valuable. More broadly, a fundamental open question is what theoretical properties are most desirable for learned regularizers, and whether the current – primarily functional analytic – viewpoint is the most appropriate for regularizers trained on finite-dimensional datasets.

7 Conclusions

In this chapter, we examined the learning of variational regularization functionals for inverse problems. We outlined the core ideas of each method, compared their strengths and limitations, and showed that most outperform traditional hand-crafted regularizers while retaining interpretability and stability. In practice, one has to balance between theoretical properties (e.g., weak convexity), computational cost, requirements on the training dataset, and reconstruction quality. Our study highlights these trade-offs, and demonstrates the performance gains enabled by more flexible architectures and increased compute resources. To ensure reproducibility, we provided key implementation details, and released the training and evaluation code online.

Looking ahead, several challenges and opportunities remain open. On the theoretical side, understanding of generalization and stability will be essential. On the practical side, more efficient training and optimization strategies are needed to enable large-scale deployment. Further, incorporating uncertainty quantification and exploring task-specific models may open promising avenues for broader applicability.

Acknowledgments

MJE acknowledges support from the EPSRC (EP/T026693/1; EP/Y037286/1). ZK acknowledges support from the EPSRC (EP/X010740/1). AD, CBS, HSW and MJE acknowledge support from the EPSRC (EP/V026259/1). JH acknowledges funding from the DFG (530824055). EK, SN and GSW acknowledge support from the DFG (SPP2298 - 543939932). EK acknowledges funding from the FWF (10.55776/COE12). SD acknowledges funding from the ERC (101020573 FunLearn). CBS acknowledges support from the Royal Society Wolfson Fellowship, the EPSRC (EP/V029428/1; ProbAI hub EP/Y028783/1), and the Wellcome Innovator Awards (215733/Z/19/Z; 221633/Z/20/Z). MJE and CBS acknowledge support from the EU Horizon 2020 research and innovation programme under the Marie Skłodowska-Curie grant agreement REMODEL. JS and ZF acknowledge funding from NIH Grant P41EB031771.

Glossary

Adam Adaptive Moment Estimation optimizer 11, 18, 20, 21

AR adversarial regularization 3, 11, 15, 19, 20, 21, 22, 23, 24, 25, 30, 31

BL-IFT bilevel learning with implicit differentiation 3, 11, 12, 13, 20, 21, 22, 24, 25, 29, 30

BL-JFB bilevel learning with Jacobian free backpropagation 3, 11, 20, 21, 22, 24, 25, 28, 29, 30

CG conjugate gradient method 12

CNN convolutional neural network 3, 4, 5, 8, 9, 10, 15, 19, 21, 22, 23, 24, 25, 26, 27

CRR convex ridge regularizer 2, 4, 5, 12, 19, 21, 22, 23, 24, 25, 26, 27, 28, 29, 30

CT computed tomography 1, 9, 18, 19, 21, 22, 24, 28, 30

DC difference-of-convex 6, 7

EM Expectation-Maximization 20

EPLL expected patch log-likelihood 3, 4, 7, 8, 16, 18, 19, 20, 21, 22, 23, 24, 25, 26, 27, 31

FBP filtered backprojection 18, 21, 22, 24, 26, 27, 28, 30

FoE fields of experts 2, 4, 5, 6, 8

GMM Gaussian mixture model 7, 16, 19

ICNN input-convex neural network 3, 4, 6, 7, 10, 19, 20, 21, 22, 23, 24, 25, 26, 27, 28, 30

IDCNN input difference-of-convex neural network 3, 4, 7, 19, 21, 22, 23, 24, 25, 26, 27, 28, 30

IFT implicit function theorem 12, 13, 19, 20, 30, 31

JFB Jacobian-free backpropagation 13, 20, 30, 31

LAR local adversarial regularization 3, 7, 8, 15, 20, 24, 25

LPD learned primal-dual 21, 22, 24, 26, 27, 28, 30

LPN learned proximal network 3, 4, 9, 10, 17, 18, 20, 21, 23, 24, 25, 26, 27, 31

LSR least-squares residual 3, 4, 9, 19, 21, 22, 23, 24, 25, 26, 27, 28, 30, 31

MAID method of adaptive inexact descent 3, 11, 13, 14, 20, 21, 22, 24, 25, 29, 30, 31

MAP maximum a-posteriori 2, 3, 15, 17

MINRES minimal residual method 12

MMSE minimum mean-squared-error 2, 3, 17

MRI magnetic resonance imaging 1, 8, 9

MSE mean squared error 20, 21, 31

NETT network Tikhonov 3, 11, 14, 15, 19, 20, 22, 24, 25, 28, 30, 31

NF normalizing flow 7, 16, 19

nmAPG nonmonotonic Accelerated Proximal Gradient algorithm 18, 23, 30, 31

PatchML patch-based maximum likelihood 7, 11, 16, 20, 24, 25

PatchNR patch normalizing flow regularizer 3, 4, 7, 8, 16, 18, 19, 20, 21, 22, 23, 24, 25, 26, 27, 31

PDHG primal-dual hybrid gradient 21

PM proximal matching 11, 17, 20, 24, 25, 31

PnP plug-and-play 3, 9, 10, 17

PSNR peak signal-to-noise ratio 19, 20, 21, 22, 24, 28, 29, 30

ReLU rectified linear unit 6, 12, 19

SM score matching [3](#), [11](#), [16](#), [17](#), [20](#), [21](#), [22](#), [23](#), [24](#), [25](#), [30](#)

TDV total deep variation [3](#), [4](#), [8](#), [9](#), [19](#), [21](#), [22](#), [23](#), [24](#), [25](#), [26](#), [27](#), [28](#), [30](#)

TV total variation [2](#), [4](#), [21](#), [22](#), [23](#), [24](#), [25](#), [31](#)

WCRR weakly-convex ridge regularizer [2](#), [4](#), [5](#), [19](#), [21](#), [22](#), [23](#), [24](#), [25](#), [26](#), [27](#), [28](#), [30](#)

References

- [1] J. Adler and O. Öktem. Learned primal-dual reconstruction. *IEEE Transactions on Medical Imaging*, 37(6):1322–1332, 2018.
- [2] H. K. Aggarwal, M. P. Mani, and M. Jacob. MoDL: Model-based deep learning architecture for inverse problems. *IEEE Transactions on Medical Imaging*, 38(2):394–405, 2018.
- [3] G. S. Alberti, E. De Vito, M. Lassas, L. Ratti, and M. Santacesaria. Learning the optimal Tikhonov regularizer for inverse problems. *Advances in Neural Information Processing Systems*, 34:25205–25216, 2021.
- [4] G. S. Alberti, J. Hertrich, M. Santacesaria, and S. Sciuotto. Manifold learning by mixture models of VAEs for inverse problems. *Journal of Machine Learning Research*, 25(202):1–35, 2024.
- [5] F. Alteküger, A. Denker, P. Hagemann, J. Hertrich, P. Maass, and G. Steidl. PatchNR: Learning from very few images by patch normalizing flow regularization. *Inverse Problems*, 39(6):064006, 2023.
- [6] B. Amos, L. Xu, and J. Z. Kolter. Input convex neural networks. In *Proceedings of the 34th International Conference on Machine Learning*, volume 70 of *Proceedings of Machine Learning Research*, pages 146–155. PMLR, 2017.
- [7] C. Anil, A. Pokle, K. Liang, J. Treutlein, Y. Wu, S. Bai, J. Z. Kolter, and R. B. Grosse. Path independent equilibrium models can better exploit test-time computation. In *Advances in Neural Information Processing Systems 35*, pages 7796–7809. Curran Associates, Inc., 2022.
- [8] S. Antholzer, J. Schwab, J. Bauer-Marschallinger, P. Burgholzer, and M. Haltmeier. NETT regularization for compressed sensing photoacoustic tomography. In *Photons Plus Ultrasound: Imaging and Sensing*, volume 10878, pages 272–282. SPIE, 2019.
- [9] V. Antun, F. Renna, C. Poon, B. Adcock, and A. C. Hansen. On instabilities of deep learning in image reconstruction and the potential costs of AI. *Proceedings of the National Academy of Sciences*, 117(48):30088–30095, 2020.
- [10] P. Arbeláez, M. Maire, C. Fowlkes, and J. Malik. Contour detection and hierarchical image segmentation. *IEEE Transactions on Pattern Analysis and Machine Intelligence*, 33(5):898–916, 2011.
- [11] L. Ardizzone, J. Kruse, C. Rother, and U. Köthe. Analyzing inverse problems with invertible neural networks. In *International Conference on Learning Representations*, 2019.
- [12] M. Arjovsky, S. Chintala, and L. Bottou. Wasserstein generative adversarial networks. In *Proceedings of the 34th International Conference on Machine Learning*, pages 214–223. PMLR, 2017.

- [13] S. G. I. Armato, G. McLennan, L. Bidaut, M. F. McNitt-Gray, C. R. Meyer, A. P. Reeves, B. Zhao, D. R. Aberle, C. I. Henschke, E. A. Hoffman, et al. The lung image database consortium (LIDC) and image database resource initiative (IDRI): A completed reference database of lung nodules on CT scans. *Medical Physics*, 38(2):915–931, 2011.
- [14] S. Arora, N. Cohen, N. Golowich, and W. Hu. A convergence analysis of gradient descent for deep linear neural networks. In *International Conference on Learning Representations*, 2019.
- [15] S. Arridge, P. Maass, O. Öktem, and C.-B. Schönlieb. Solving inverse problems using data-driven models. *Acta Numerica*, 28:1–174, 2019.
- [16] S. Bai, J. Z. Kolter, and V. Koltun. Deep equilibrium models. In *Advances in Neural Information Processing Systems 32*, pages 1–12. Curran Associates, Inc., 2019.
- [17] S. Bai, V. Koltun, and Z. Kolter. Stabilizing equilibrium models by Jacobian regularization. In *Proceedings of the 38th International Conference on Machine Learning*, pages 554–565. PMLR, 2021.
- [18] P. F. Baldi and K. Hornik. Learning in linear neural networks: A survey. *IEEE Transactions on Neural Networks*, 6(4):837–858, 1995.
- [19] J. T. Barron. Continuously differentiable exponential linear units. *arXiv preprint arXiv:1704.07483*, 2017.
- [20] A. Beck and M. Teboulle. A fast iterative shrinkage-thresholding algorithm for linear inverse problems. *SIAM Journal on Imaging Sciences*, 2(1):183–202, 2009.
- [21] S. Becker and G. E. Hinton. Self-organizing neural network that discovers surfaces in random-dot stereograms. *Nature*, 355(6356):161–163, 1992.
- [22] Y. Bengio. Gradient-based optimization of hyperparameters. *Neural Computation*, 12(8):1889–1900, 2000.
- [23] M. Benning and M. Burger. Modern Regularization Methods for Inverse Problems. *Acta Numerica*, 27:1–111, 2018.
- [24] D. Bianchi, G. Lai, and W. Li. Uniformly convex neural networks and non-stationary iterated network (iNETT) method. *Inverse Problems*, 39(5):055002, 2023.
- [25] S. Bigdeli and M. Zwicker. Image restoration using autoencoding priors. In *Proceedings of the 13th International Joint Conference on Computer Vision, Imaging and Computer Graphics Theory and Applications*, pages 33–44, 2018.
- [26] J. Bolte and E. Pauwels. Conservative set valued fields, automatic differentiation, stochastic gradient methods and deep learning. *Mathematical Programming*, 188(1):19–51, 2021.
- [27] J. Bolte, E. Pauwels, and S. Vaiter. One-step differentiation of iterative algorithms. In *Advances in Neural Information Processing Systems 36*. Curran Associates, Inc., 2023.
- [28] A. Bora, A. Jalal, E. Price, and A. G. Dimakis. Compressed sensing using generative models. In *Proceedings of the 34th International Conference on Machine Learning*, pages 537–546. PMLR, 2017.
- [29] A. M. Bruckstein, D. L. Donoho, and M. Elad. From sparse solutions of systems of equations to sparse modeling of signals and images. *SIAM Review*, 51(1):34–81, 2009.

[30] A. Buades, B. Coll, and J.-M. Morel. A review of image denoising algorithms, with a new one. *Multiscale Modeling & Simulation*, 4(2):490–530, 2005.

[31] L. Calatroni, C. Cao, J. C. De Los Reyes, C.-B. Schönlieb, and T. Valkonen. Bilevel approaches for learning of variational imaging models. In *Variational Methods: In Imaging and Geometric Control*, pages 252–290. Walter de Gruyter, 2017.

[32] A. Chambolle and T. Pock. A first-order primal-dual algorithm for convex problems with applications to imaging. *Journal of Mathematical Imaging and Vision*, 40(1):120–145, 2011.

[33] S. H. Chan, X. Wang, and O. A. Elgendi. Plug-and-Play ADMM for image restoration: Fixed-point convergence and applications. *IEEE Transactions on Computational Imaging*, 3(1):84–98, 2016.

[34] T. Chen, X. Chen, W. Chen, H. Heaton, J. Liu, Z. Wang, and W. Yin. Learning to optimize: A primer and a benchmark. *Journal of Machine Learning Research*, 23(189):1–59, 2022.

[35] T. Chen, S. Kornblith, M. Norouzi, and G. Hinton. A simple framework for contrastive learning of visual representations. In *Proceedings of the 37th International Conference on Machine Learning*, pages 1597–1607. PMLR, 2020.

[36] D.-A. Clevert, T. Unterthiner, and S. Hochreiter. Fast and accurate deep network learning by exponential linear units (ELUs). In *International Conference on Learning Representations*, 2016.

[37] R. Cohen, Y. Blau, D. Freedman, and E. Rivlin. It has potential: Gradient-driven denoisers for convergent solutions to inverse problems. In *Advances in Neural Information Processing Systems 34*, pages 18152–18164. Curran Associates, Inc., 2021.

[38] K. Dabov, A. Foi, V. Katkovnik, and K. Egiazarian. Image denoising by sparse 3-D transform-domain collaborative filtering. *IEEE Transactions on Image Processing*, 16(8):2080–2095, 2007.

[39] J. C. De los Reyes and C.-B. Schönlieb. Image denoising: Learning the noise model via nonsmooth PDE-constrained optimization. *Inverse Problems and Imaging*, 7(4):1183–1214, 2013.

[40] J. C. De los Reyes, C.-B. Schönlieb, and T. Valkonen. Bilevel parameter learning for higher-order total variation regularisation models. *Journal of Mathematical Imaging and Vision*, 57(1):1–25, 2017.

[41] C.-A. Deledalle, S. Parameswaran, and T. Q. Nguyen. Image denoising with generalized Gaussian mixture model patch priors. *SIAM Journal on Imaging Sciences*, 11(4):2568–2609, 2018.

[42] A. Denker, M. Schmidt, J. Leuschner, and P. Maass. Conditional invertible neural networks for medical imaging. *Journal of Imaging*, 7(11):243, 2021.

[43] L. Dinh, J. Sohl-Dickstein, and S. Bengio. Density estimation using real NVP. In *International Conference on Learning Representations*, 2017.

[44] J. Duchi, E. Hazan, and Y. Singer. Adaptive subgradient methods for online learning and stochastic optimization. *Journal of Machine Learning Research*, 12(61):2121–2159, 2011.

[45] S. Ducotterd, A. Goujon, P. Bohra, D. Perdios, S. Neumayer, and M. Unser. Improving Lipschitz-constrained neural networks by learning activation functions. *Journal of Machine Learning Research*, 25(65):1–30, 2024.

[46] M. A. G. Duff, N. D. F. Campbell, and M. J. Ehrhardt. Regularising inverse problems with generative machine learning models. *Journal of Mathematical Imaging and Vision*, 66:37–56, 2024.

[47] B. Efron. Tweedie’s formula and selection bias. *Journal of the American Statistical Association*, 106(496):1602–1614, 2011.

[48] M. J. Ehrhardt and L. Roberts. Analyzing inexact hypergradients for bilevel learning. *IMA Journal of Applied Mathematics*, 89(1):254–278, 2024.

[49] J. Fan and R. Li. Variable selection via nonconcave penalized likelihood and its oracle properties. *Journal of the American Statistical Association*, 96(456):1348–1360, 2001.

[50] Z. Fang, S. Buchanan, and J. Sulam. What’s in a prior? Learned proximal networks for inverse problems. In *International Conference on Learning Representations*, 2024.

[51] R. Fermanian, M. Le Pendu, and C. Guillemot. PnP-ReG: Learned regularizing gradient for plug-and-play gradient descent. *SIAM Journal on Imaging Sciences*, 16(2):585–613, 2023.

[52] S. W. Fung, H. Heaton, Q. Li, D. Mckenzie, S. Osher, and W. Yin. JFB: Jacobian-free back-propagation for implicit networks. *Proceedings of the AAAI Conference on Artificial Intelligence*, 36(6):6648–6656, 2022.

[53] I. J. Goodfellow, J. Pouget-Abadie, M. Mirza, B. Xu, D. Warde-Farley, S. Ozair, A. Courville, and Y. Bengio. Generative adversarial nets. In *Advances in Neural Information Processing Systems 27*. Curran Associates, Inc., 2014.

[54] N. M. Gottschling, V. Antun, A. C. Hansen, and B. Adcock. The troublesome kernel: On hallucinations, no free lunches, and the accuracy-stability tradeoff in inverse problems. *SIAM Review*, 67(1):73–104, 2025.

[55] A. Goujon, S. Neumayer, P. Bohra, S. Ducotterd, and M. Unser. A neural-network-based convex regularizer for inverse problems. *IEEE Transactions on Computational Imaging*, 9:781–795, 2023.

[56] A. Goujon, S. Neumayer, and M. Unser. Learning weakly convex regularizers for convergent image-reconstruction algorithms. *SIAM Journal on Imaging Sciences*, 17(1):91–115, 2024.

[57] R. Graffi, L. Franceschi, M. Pontil, and S. Salzo. On the iteration complexity of hypergradient computation. In *Proceedings of the 37th International Conference on Machine Learning*, pages 3748–3758. PMLR, 2020.

[58] R. Gribonval and M. Nikolova. A characterization of proximity operators. *Journal of Mathematical Imaging and Vision*, 62(6-7):773–789, 2020.

[59] A. Gruslys, R. Munos, I. Danihelka, M. Lanctot, and A. Graves. Memory-efficient backpropagation through time. In *Advances in Neural Information Processing Systems 29*. Curran Associates, Inc., 2016.

[60] E. Haber, L. Horesh, and L. Tenorio. Numerical methods for the design of large-scale nonlinear discrete ill-posed inverse problems. *Inverse Problems*, 26(2):025002, 2009.

[61] A. Habring, A. Falk, M. Zach, and T. Pock. Diffusion at absolute zero: Langevin sampling using successive moreau envelopes. *arXiv Preprint arXiv:2503.22258*, 2025.

[62] A. Habring and M. Holler. A generative variational model for inverse problems in imaging. *SIAM Journal on Mathematics of Data Science*, 4(1):306–335, 2022.

[63] A. Habring and M. Holler. Neural-network-based regularization methods for inverse problems in imaging. *GAMM-Mitteilungen*, 47(4):e202470004, 2024.

[64] J. Hadamard. *Lectures on Cauchy's Problem in Linear Partial Differential Equations*. Yale University Press, 1923.

[65] M. Hasannasab, J. Hertrich, S. Neumayer, G. Plonka, S. Setzer, and G. Steidl. Parseval proximal neural networks. *The Journal of Fourier Analysis*, 26:59, 2020.

[66] T. Hastie, R. Tibshirani, and J. Friedman. *The Elements of Statistical Learning: Data Mining, Inference, and Prediction*. Springer, 2009.

[67] A. Hauptmann, J. Adler, S. Arridge, and O. Öktem. Multi-scale learned iterative reconstruction. *IEEE Transactions on Computational Imaging*, 6:843–856, 2020.

[68] L. Helminger, M. Bernasconi, A. Djelouah, M. Gross, and C. Schroers. Generic image restoration with flow based priors. In *Proceedings of the IEEE/CVF Conference on Computer Vision and Pattern Recognition*, pages 334–343, 2021.

[69] D. Hendrycks and K. Gimpel. Gaussian error linear units (GELU). *arXiv Preprint arXiv:1606.08415*, 2016.

[70] J. Hertrich, S. Neumayer, and G. Steidl. Convolutional proximal neural networks and Plug-and-Play algorithms. *Linear Algebra and Applications*, 631:203–234, 2021.

[71] G. E. Hinton. Training products of experts by minimizing contrastive divergence. *Neural Computation*, 14(8):1771–1800, 2002.

[72] A. Houdard, C. Bouveyron, and J. Delon. High-dimensional mixture models for unsupervised image denoising (HDMI). *SIAM Journal on Imaging Sciences*, 11(4):2815–2846, 2018.

[73] J. Hu, B. Song, X. Xu, L. Shen, and J. A. Fessler. Learning image priors through patch-based diffusion models for solving inverse problems. In *Advances in Neural Information Processing Systems 37*, pages 1625–1660. Curran Associates, Inc., 2024.

[74] S. Hurault, A. Leclaire, and N. Papadakis. Gradient step denoiser for convergent Plug-and-Play. In *International Conference on Learning Representations*, 2022.

[75] S. Hurault, A. Leclaire, and N. Papadakis. Proximal denoiser for convergent Plug-and-Play optimization with nonconvex regularization. In *Proceedings of the 39th International Conference on Machine Learning*, pages 9483–9505. PMLR, 2022.

[76] A. Hyvärinen. Estimation of non-normalized statistical models by score matching. *Journal of Machine Learning Research*, 6(24):695–709, 2005.

[77] K. Ito and B. Jin. *Inverse Problems: Tikhonov Theory and Algorithms*. World Scientific, 2014.

[78] K. Ji, J. Yang, and Y. Liang. Bilevel optimization: Convergence analysis and enhanced design. In *Proceedings of the 38th International Conference on Machine Learning*, pages 4882–4892. PMLR, 2021.

[79] K. H. Jin, M. T. McCann, E. Froustey, and M. Unser. Deep convolutional neural network for inverse problems in imaging. *IEEE Transactions on Image Processing*, 26(9):4509–4522, 2017.

[80] B. Kawar, M. Elad, S. Ermon, and J. Song. Denoising diffusion restoration models. In *Advances in Neural Information Processing Systems 35*, pages 23593–23606. Curran Associates, Inc., 2022.

[81] D. P. Kingma and J. Ba. Adam: A method for stochastic optimization. In *International Conference on Learning Representations*, 2015.

[82] E. Kobler, A. Effland, K. Kunisch, and T. Pock. Total deep variation for linear inverse problems. In *Proceedings of the IEEE/CVF Conference on Computer Vision and Pattern Recognition*, 2020.

[83] E. Kobler, A. Effland, K. Kunisch, and T. Pock. Total deep variation: A stable regularization method for inverse problems. *IEEE Transactions on Pattern Analysis and Machine Intelligence*, 44(12):9163–9180, 2021.

[84] A. Kofler, F. Altekrüger, F. A. Ba, C. Kolbitsch, E. Papoutsellis, D. Schote, C. Sirotenko, F. F. Zimmermann, and K. Papafitsoros. Learning regularization parameter-maps for variational image reconstruction using deep neural networks and algorithm unrolling. *SIAM Journal on Imaging Sciences*, 16(4):2202–2246, 2023.

[85] K. Kunisch and T. Pock. A bilevel optimization approach for parameter learning in variational models. *SIAM Journal on Imaging Sciences*, 6(2):938–983, 2013.

[86] M. Kuric, M. Zach, A. Habring, M. Unser, and T. Pock. The Gaussian latent machine: Efficient prior and posterior sampling for inverse problems. *arXiv Preprint arXiv:2505.12836*, 2025.

[87] R. Laumont, V. D. Bortoli, A. Almansa, J. Delon, A. Durmus, and M. Pereyra. Bayesian imaging using plug & play priors: When Langevin meets Tweedie. *SIAM Journal on Imaging Sciences*, 15(2):701–737, 2022.

[88] H. A. Le Thi and T. Pham Dinh. DC programming and DCA: Thirty years of developments. *Mathematical Programming*, 169(1):5–68, 2018.

[89] J. Leuschner, M. Schmidt, D. O. Baguer, and P. Maass. LoDoPaB-CT, a benchmark dataset for low-dose computed tomography reconstruction. *Scientific Data*, 8(1):109, 2021.

[90] H. Li and Z. Lin. Accelerated proximal gradient methods for nonconvex programming. In *Advances in Neural Information Processing Systems 28*. Curran Associates, Inc., 2015.

[91] H. Li, J. Schwab, S. Antholzer, and M. Haltmeier. NETT: Solving inverse problems with deep neural networks. *Inverse Problems*, 36(6):065005, 2020.

[92] R. Liao, Y. Xiong, E. Fetaya, L. Zhang, K. Yoon, X. Pitkow, R. Urtasun, and R. Zemel. Reviving and improving recurrent back-propagation. In *Proceedings of the 35th International Conference on Machine Learning*, pages 3082–3091. PMLR, 2018.

[93] S. Lunz, O. Öktem, and C.-B. Schönlieb. Adversarial regularizers in inverse problems. In *Advances in Neural Information Processing Systems 31*. Curran Associates, Inc., 2018.

[94] J. Mairal, J. Ponce, G. Sapiro, A. Zisserman, and F. Bach. Supervised dictionary learning. In *Advances in Neural Information Processing Systems 21*. Curran Associates, Inc., 2008.

[95] D. Martin, C. Fowlkes, D. Tal, and J. Malik. A database of human segmented natural images and its application to evaluating segmentation algorithms and measuring ecological statistics. In *Proceedings of the 8th International Conference on Computer Vision*, pages 416–423, 2001.

[96] R. Mazumder, J. H. Friedman, and T. Hastie. Sparsenet: Coordinate descent with nonconvex penalties. *Journal of the American Statistical Association*, 106(495):1125–1138, 2011.

[97] S. Mehmood and P. Ochs. Automatic differentiation of some first-order methods in parametric optimization. In *International Conference on Artificial Intelligence and Statistics*, pages 1584–1594. PMLR, 2020.

[98] K. Miyasawa. An empirical Bayes estimator of the mean of a normal population. *Bulletin of the International Statistical Institute*, 38(181-188):1–2, 1961.

[99] V. Monga, Y. Li, and Y. C. Eldar. Algorithm unrolling: Interpretable, efficient deep learning for signal and image processing. *IEEE Signal Processing Magazine*, 38(2):18–44, 2021.

[100] J.-J. Moreau. Proximité et dualité dans un espace Hilbertien. *Bulletin de la Société mathématique de France*, 93:273–299, 1965.

[101] S. Mukherjee, S. Dittmer, Z. Shumaylov, S. Lunz, O. Öktem, and C.-B. Schönlieb. Learned convex regularizers for inverse problems. *arXiv:2008.02839*, 2021.

[102] S. Mukherjee, A. Hauptmann, O. Öktem, M. Pereyra, and C.-B. Schönlieb. Learned reconstruction methods with convergence guarantees: A survey of concepts and applications. *IEEE Signal Processing Magazine*, 40(1):164–182, 2023.

[103] S. Mukherjee, C.-B. Schönlieb, and M. Burger. Learning convex regularizers satisfying the variational source condition for inverse problems. In *NeurIPS Workshops*, 2021.

[104] D. Narnhofer, A. Effland, E. Kobler, K. Hammernik, F. Knoll, and T. Pock. Bayesian uncertainty estimation of learned variational MRI reconstruction. *IEEE Transactions on Medical Imaging*, 41(2):279–291, 2021.

[105] S. Neumayer and F. Altekrüger. Stability of data-dependent ridge-regularization for inverse problems. *Inverse Problems*, 41(6):065006, 2025.

[106] S. Neumayer, M. Pourya, A. Goujon, and M. Unser. Boosting weakly convex ridge regularizers with spatial adaptivity. In *NeurIPS Workshop Deep Inverse*, 2023.

[107] D.-P.-L. Nguyen, J. Hertrich, J.-F. Aujol, and Y. Berthoumieu. Image super-resolution with PCA reduced generalized Gaussian mixture models in materials science. *Inverse Problems and Imaging*, 17(6):1165–1192, 2023.

[108] M. Nikolova. Energy minimization methods. In *Handbook of Mathematical Methods in Imaging*, pages 157–204. Springer, New York, 2015.

[109] D. Obmann, L. Nguyen, J. Schwab, and M. Haltmeier. Augmented NETT regularization of inverse problems. *Journal of Physics Communications*, 5(10):105002, 2021.

[110] P. Ochs, R. Ranftl, T. Brox, and T. Pock. Techniques for gradient-based bilevel optimization with non-smooth lower level problems. *Journal of Mathematical Imaging and Vision*, 56:175–194, 2016.

[111] G. Ongie, A. Jalal, C. A. Metzler, R. G. Baraniuk, A. G. Dimakis, and R. Willett. Deep learning techniques for inverse problems in imaging. *IEEE Journal on Selected Areas in Information Theory*, 1(1):39–56, 2020.

[112] V. Palyan and M. Elad. Multi-scale patch-based image restoration. *IEEE Transactions on Image Processing*, 25(1):249–261, 2015.

- [113] S. Parameswaran, C.-A. Deledalle, L. Denis, and T. Q. Nguyen. Accelerating GMM-based patch priors for image restoration: Three ingredients for a 100x speed-up. *IEEE Transactions on Image Processing*, 28(2):687–698, 2018.
- [114] F. Pedregosa. Hyperparameter optimization with approximate gradient. In *Proceedings of the 33rd International Conference on Machine Learning*, pages 737–746. PMLR, 2016.
- [115] J.-C. Pesquet, A. Repetti, M. Terris, and Y. Wiaux. Learning maximally monotone operators for image recovery. *SIAM Journal on Imaging Sciences*, 14(3):1206–1237, 2021.
- [116] M. Piening, F. Alteküger, J. Hertrich, P. Hagemann, A. Walther, and G. Steidl. Learning from small data sets: Patch-based regularizers in inverse problems for image reconstruction. *GAMM-Mitteilungen*, 47(4):e202470002, 2024.
- [117] T. Pinetz, E. Kobler, C. Doberstein, B. Berkels, and A. Effland. Total deep variation for noisy exit wave reconstruction in transmission electron microscopy. In *International Conference on Scale Space and Variational Methods in Computer Vision*, pages 491–502, 2021.
- [118] T. Pinetz, E. Kobler, T. Pock, and A. Effland. Shared prior learning of energy-based models for image reconstruction. *SIAM Journal on Imaging Sciences*, 14(4):1706–1748, 2021.
- [119] T. Pock, D. Cremers, H. Bischof, and A. Chambolle. An algorithm for minimizing the Mumford-Shah functional. In *IEEE International Conference on Computer Vision*, pages 1133–1140. IEEE, 2009.
- [120] M. Pourya, E. Kobler, M. Unser, and S. Neumayer. DEALing with image reconstruction: Deep attentive least squares. In *Proceedings of the 42nd International Conference on Machine Learning*. PMLR, 2025.
- [121] M. Pourya, S. Neumayer, and M. Unser. Iteratively refined image reconstruction with learned attentive regularizers. *Numerical Functional Analysis and Optimization*, 45(7–9):411–440, 2024.
- [122] J. Prost, A. Houdard, A. Almansa, and N. Papadakis. Learning local regularization for variational image restoration. In *International Conference on Scale Space and Variational Methods in Computer Vision*, pages 358–370. Springer, 2021.
- [123] A. Radford, J. W. Kim, C. Hallacy, A. Ramesh, G. Goh, S. Agarwal, G. Sastry, A. Askell, P. Mishkin, J. Clark, et al. Learning transferable visual models from natural language supervision. In *Proceedings of the 38th International Conference on Machine Learning*, pages 8748–8763. PMLR, 2021.
- [124] E. T. Reehorst and P. Schniter. Regularization by denoising: Clarifications and new interpretations. *IEEE Transactions on Computational Imaging*, 5(1):52–67, 2018.
- [125] A. Ribes and F. Schmitt. Linear inverse problems in imaging. *IEEE Signal Processing Magazine*, 25(4):84–99, 2008.
- [126] H. E. Robbins. An empirical Bayes approach to statistics. In *Breakthroughs in Statistics: Foundations and Basic Theory*, pages 388–394. Springer, NY, 1992.
- [127] Y. Romano, M. Elad, and P. Milanfar. The little engine that could: Regularization by denoising (RED). *SIAM Journal on Imaging Sciences*, 10(4):1804–1844, 2017.
- [128] R. Rombach, A. Blattmann, D. Lorenz, P. Esser, and B. Ommer. High-resolution image synthesis with latent diffusion models. In *Proceedings of the IEEE/CVF Conference on Computer Vision and Pattern Recognition*, pages 10684–10695, 2022.

[129] O. Ronneberger, P. Fischer, and T. Brox. U-net: Convolutional networks for biomedical image segmentation. In *Proceedings of Medical Image Computing and Computer-Assisted Intervention 2015, Part III*, pages 234–241. Springer, 2015.

[130] S. Roth and M. J. Black. Fields of experts. *International Journal of Computer Vision*, 82(2):205–229, 2009.

[131] L. I. Rudin, S. Osher, and E. Fatemi. Nonlinear total variation based noise removal algorithms. *Physica D: Nonlinear Phenomena*, 60(1-4):259–268, 1992.

[132] M. S. Salehi, S. Mukherjee, L. Roberts, and M. J. Ehrhardt. An adaptively inexact first-order method for bilevel optimization with application to hyperparameter learning. *SIAM Journal on Mathematics of Data Science*, 7(3):906–936, 2025.

[133] M. S. Salehi, S. Mukherjee, L. Roberts, and M. J. Ehrhardt. Bilevel learning with inexact stochastic gradients. In *International Conference on Scale Space and Variational Methods in Computer Vision*, pages 347–359. Springer, 2025.

[134] K. G. Samuel and M. F. Tappen. Learning optimized MAP estimates in continuously-valued MRF models. In *Proceedings of the IEEE/CVF Conference on Computer Vision and Pattern Recognition*, pages 477–484, 2009.

[135] O. Scherzer, M. Grasmair, H. Grossauer, M. Haltmeier, and F. Lenzen. *Variational Methods in Imaging*. Springer, 2009.

[136] A. Shaban, C.-A. Cheng, N. Hatch, and B. Boots. Truncated back-propagation for bilevel optimization. In *Proceedings of the 22nd International Conference on Artificial Intelligence and Statistics*, pages 1723–1732. PMLR, 2019.

[137] Z. Shumaylov, J. Budd, S. Mukherjee, and C.-B. Schönlieb. Provably convergent data-driven convex-nonconvex regularization. In *NeurIPS Workshop Deep Inverse*, 2023.

[138] Z. Shumaylov, J. Budd, S. Mukherjee, and C.-B. Schönlieb. Weakly convex regularisers for inverse problems: Convergence of critical points and primal-dual optimisation. In *Proceedings of the 41st International Conference on Machine Learning*. PMLR, 2024.

[139] Y. Song and S. Ermon. Generative modeling by estimating gradients of the data distribution. In *Advances in Neural Information Processing Systems 32*. Curran Associates, Inc., 2019.

[140] J. Sulam and M. Elad. Expected patch log likelihood with a sparse prior. In *International Conference on Energy Minimization Methods in Computer Vision and Pattern Recognition*, pages 99–111. Springer, 2015.

[141] J. Tachella, M. Terris, S. Hurault, A. Wang, D. Chen, M.-H. Nguyen, M. Song, T. Davies, L. Davy, J. Dong, P. Escande, J. Hertrich, Z. Hu, T. I. Liaudat, N. Laurent, B. Levac, M. Massias, T. Moreau, T. Modrzyk, B. Monroy, S. Neumayer, J. Scanvic, F. Sarron, V. Sechaud, G. Schramm, C. Tang, R. Vo, and P. Weiss. DeepInverse: A Python package for solving imaging inverse problems with deep learning. *arXiv preprint arXiv:2505.20160*, 2025.

[142] H. Y. Tan, Z. Cai, M. Pereyra, S. Mukherjee, J. Tang, and C.-B. Schönlieb. Unsupervised training of convex regularizers using maximum likelihood estimation. *Transactions on Machine Learning Research*, 2024.

[143] I. Tošić and P. Frossard. Dictionary learning. *IEEE Signal Processing Magazine*, 28(2):27–38, 2011.

[144] S. C. Tudosie, A. Denker, Z. Kereta, and S. Arridge. Learning binary sampling patterns for single-pixel imaging using bilevel optimisation. *arXiv preprint arXiv:2508.19068*, 2025.

[145] S. V. Venkatakrishnan, C. A. Bouman, and B. Wohlberg. Plug-and-play priors for model based reconstruction. In *IEEE Global Conference on Signal and Information Processing*, pages 945–948, 2013.

[146] P. Vicol, L. Metz, and J. Sohl-Dickstein. Unbiased gradient estimation in unrolled computation graphs with persistent evolution strategies. In *Proceedings of the 38th International Conference on Machine Learning*, pages 10553–10563. PMLR, 2021.

[147] P. Vincent. A connection between score matching and denoising autoencoders. *Neural Computation*, 23(7):1661–1674, 2011.

[148] G. Wang, J. C. Ye, and B. De Man. Deep learning for tomographic image reconstruction. *Nature Machine Intelligence*, 2(12):737–748, 2020.

[149] J. Wang, J. Fan, B. Zhou, X. Huang, and L. Chen. Hybrid reconstruction of the physical model with the deep learning that improves structured illumination microscopy. *Advanced Photonics Nexus*, 2(1):016012–016012, 2023.

[150] R. Ward, X. Wu, and L. Bottou. AdaGrad stepsizes: Sharp convergence over nonconvex landscapes. In *Proceedings of the 36th International Conference on Machine Learning*, pages 6677–6686. PMLR, 2019.

[151] X. Wei, H. Van Gorp, L. Gonzalez-Carabarin, D. Freedman, Y. C. Eldar, and R. J. van Sloun. Deep unfolding with normalizing flow priors for inverse problems. *IEEE Transactions on Signal Processing*, 70:2962–2971, 2022.

[152] P. Yin, Y. Lou, Q. He, and J. Xin. Minimization of ℓ_{1-2} for compressed sensing. *SIAM Journal on Scientific Computing*, 37(1):A536–A563, 2015.

[153] M. Zach, F. Knoll, and T. Pock. Stable deep MRI reconstruction using generative priors. *IEEE Transactions on Medical Imaging*, 2023.

[154] M. Zach, E. Kobler, A. Chambolle, and T. Pock. Product of Gaussian mixture diffusion models. *Journal of Mathematical Imaging and Vision*, pages 1–25, 2024.

[155] M. Zach, E. Kobler, and T. Pock. Computed tomography reconstruction using generative energy-based priors. In *OAGM Workshop*, pages 52–58, 2021.

[156] C.-H. Zhang. Nearly unbiased variable selection under minimax concave penalty. *The Annals of Statistics*, 38(2):894–942, 2010.

[157] K. Zhang, Y. Li, W. Zuo, L. Zhang, L. V. Gool, and R. Timofte. Plug-and-play image restoration with deep denoiser prior. *IEEE Transactions on Pattern Analysis and Machine Intelligence*, 44(10):6360–6376, 2022.

[158] R. Zhang. Making convolutional networks shift-invariant again. In *Proceedings of the 36th International Conference on Machine Learning*, pages 7324–7334. PMLR, 2019.

[159] R. Zhang, P. Isola, A. A. Efros, E. Shechtman, and O. Wang. The unreasonable effectiveness of deep features as a perceptual metric. In *Proceedings of the IEEE/CVF Conference on Computer Vision and Pattern Recognition*, pages 586–595, 2018.

- [160] Y. Zhang and O. Leong. Learning difference-of-convex regularizers for inverse problems: A flexible framework with theoretical guarantees. *arXiv preprint arXiv:2502.00240*, 2025.
- [161] J. Zhuang, T. Tang, Y. Ding, S. C. Tatikonda, N. Dvornek, X. Papademetris, and J. Duncan. Adabelief optimizer: Adapting stepsizes by the belief in observed gradients. In *Advances in Neural Information Processing Systems 33*, pages 18795–18806. Curran Associates, Inc., 2020.
- [162] D. Zoran and Y. Weiss. From learning models of natural image patches to whole image restoration. In *IEEE International Conference on Computer Vision*, pages 479–486, 2011.
- [163] Z. Zou, J. Liu, B. Wohlberg, and U. S. Kamilov. Deep equilibrium learning of explicit regularization functionals for imaging inverse problems. *IEEE Open Journal of Signal Processing*, 4:390–398, 2023.
- [164] N. Zucchetti and J. Sacramento. Beyond backpropagation: Bilevel optimization through implicit differentiation and equilibrium propagation. *Neural Computation*, 34(12):2309–2346, 2022.